Seismic Capacity and Multi-Mechanism Analysis for Dry-Stack Masonry Arches Subjected to Hinge Control

Gabriel L. Stockdale[1*], Vasilis Sarhosis[2], and Gabriele Milani[1]

[1] Dept. of Architecture, Built Environment and Construction Engineering, Politecnico di Milano
Piazza Leonardo da Vinci 32, 20133 Milan, Italy
e-mail: gabriellee.stockdale@polimi.it*; gabriele.milani@polimi.it
* Corresponding author

[2] School of Engineering, Newcastle University
Newcastle upon Tyne, NE1 7RU, UK
e-mail: vasilis.sarhosis@newcastle.ac.uk

Abstract

Masonry arches are vulnerable to seismic actions. Over the last few years, extensive research has been carried out to develop strategies and methods for their seismic assessment and strengthening. The application of constant horizontal accelerations to masonry arches is a well-known quasi-static method, which approximates dynamic loading effects and quantifies their stability, while tilting plane testing is a cheap and effective strategy for experimentation of arches made of dry-stack masonry. Also, the common strengthening techniques for masonry arches are mainly focusing on achieving full strength of the system rather than stability. Through experimentation of a dry-stack masonry arch it has been shown that the capacity of an arch can be increased, and the failure controlled by defining hinge positions through reinforcement. This paper utilizes experimentally obtained results to introduce: (1) static friction and resulting mechanisms; and (2) the post-minimum mechanism reinforcement requirements into the two-dimensional limit analysis-based kinematic collapse load calculator (KCLC) software designed for the static seismic analysis of dry-stack masonry arches. Computational results are validated against a series of experimental observations based on tilt plane tests and good agreement is obtained. Discrete Element models to represent the masonry arch with different hinge configurations are also developed to establish a validation trifecta. The limiting mechanism to activate collapse of arches subjected to hinge control is investigated and insights into the optimal reinforcement to be installed in the arch are derived. It is envisaged that the current modelling approach can be used by engineers to understand stability under horizontal loads and develop strengthening criteria for masonry arches of their care.

Keywords: Masonry Arch; Tilt Test; KCLC; DEM; Admissible Mechanism; Seismic Capacity

1 Introduction

Seismic assessment and retrofitting of masonry arches is critical for both preservation and safety. Full-scale non-linear dynamic testing and analysis is often required to understand the true behaviours of an arch under seismic loading, but such approaches are time consuming and expensive to implement. As an alternative, static assessment strategies have been employed by several researchers in the past with sufficient success. For static seismic assessments, the condition of constant horizontal acceleration is often utilized, and the tilting plane test has been proven to be a cheap and effective strategy to impose static horizontal accelerations to an arch (DeJong 2009). However, the tilting plane decomposes gravity instead of adding acceleration and ultimately changes the system. While these changes do not alter the capacity of an arch, the stresses are reduced which could have an effect when non-ideal conditions are considered.

There does exist a significant amount of analysis tools, techniques, and experimental investigations aimed at the assessment of arches and existing structures (Sarhosis et al. 2016b; Tralli et al. 2014; Hendry 1998). For earthquake loading, the commonly used techniques are divided into limit analysis (LA) and numerical analyses approaches. The LA approaches include the upper and lower bound theorems. The lower bound theorem, states that an arch is stable if there exists a thrust line that lies entirely within the boundary of the arch. The thrust line analysis is derived from Hooke's hanging chain analogy, solidified in Heyman's safe theorem, and has been utilized to impose static horizontal testing through the gravity decomposition of a tilting plane (DeJong 2009; Huerta 2005; Heyman 1969). The upper bound theorem, or kinematic theorem states that an arch will fail if a kinematically admissible mechanism exists that produces positive or zero work from external forces. This approach applies equivalent horizontal accelerations and an iterative approach to the principles of virtual work to determine collapse (Clemente 1998; Gilbert and Melborn 1994; Oppenheim 1992). The lower bound tilting plane analysis utilized by DeJong (2009) produced results in agreement with the upper bound results previously obtained by Clemente (1998) and Oppenheim (1992). Additionally, the kinematic theorem with lateral loading has been validated both numerically and experimentally (Dimitri and Tornabene 2015; Alexakis and Makris 2014; De Luca et al. 2004; Ochsendorf 2002); which in turn argues the validity of the tilting plane analysis for the kinematic theorem.

The numerical approaches used to simulate earthquake loading in masonry arches are divided into two main categories: a) non-linear finite element method (FEM); and b) the distinct (or discrete) element method (DEM). The discontinuous nature of masonry does not allow it to be modelled in the elastic continuum and thus requires the non-linear analysis (Dimitri and Tornabene 2015). The non-linear FEM analysis requires a high level of expertise to employ and is computationally expensive. Nonetheless, it has been successfully applied in both static pushover and non-linear dynamic cases (Formisano and Marzo 2017; Gaetani et al. 2016; Pelà 2015; Zampieri 2015; Krstevska et al. 2010; Pelà et al. 2009; Fanning, et al.2005). DEM was originally used in rock engineering where continuity does not exist and has been used for simulating the mechanical behaviour of masonry structures (Sarhosis et al. 2014; Giamundo et al. 2014; Forgacs et al. 2017; Bui et al. 2017; Cundal 1971). DEM relies on the principles of Newtonian laws of motion to characterize the position and velocity of each block. In particular, the calculations are made using the force-displacement law at all contacts and the Newton's second law of motion at all blocks. The force-displacement law is used to find contact forces from known displacements, while Newton's second law governs the motion of the blocks resulting from the known forces acting on them. The movement and deformations of the blocks are traced per time step which results in the ability to examine the progressive development of collapse (3DEC 2015; Sarhosis et al. 2016a, Dimitri and Tornabene 2015; DeJong 2009; DeJong et al. 2008; De Lorenzis et al. 2007). As with the non-linear FEM, DEM requires a high level of expertise and computational costs (Sarhosis et al. 2016c).

Today, a comprehensive understanding of the seismic behaviour of arches exists as well as the ability to analyse most situations. The problem is the accessibility of that understanding and the efficiency at which it can be applied. Both LA approaches examine earthquake loading through statics and are limited to the onset of a mechanism. They cannot predict the post-stable dynamic response, but if the mechanism is not engaged, then neither is the dynamic rocking (DeJong et al. 2008; De Lorenzis et al. 2007). Therefore, both LA approaches produce conservative results, and coupled with the simplicity and speed at which results can be obtained emphasise a strong justification for their use in standard seismic assessments of masonry arches.

In addition to the tools and techniques of assessment, there also exists a strong understanding of reinforcement and retrofitting strategies for masonry arches (Heydariha et al 2019; Alexandros et al. 2018; Bertolesi et al. 2018; Carozzi et al. 2018; Ceroni and Salzano 2018; De Santis et al. 2018; Modena et al. 2015; Bhattacharya et al. 2014; Calderini and Lagomarsino 2014). Of the various techniques, fibre reinforced polymers (FRP) and textile reinforced

mortars (TRM) are strategies that have proven their adeptness for reinforcing flexural hinges and their ease of installation. Their application however is typically done such that the arch's failure transforms from the traditional mechanism to a material strength problem (i.e. delamination, rupture or crushing) (Bertolesi et al. 2018, Carozzi et al. 2018; De Santis et al. 2018; Anania and D'Agata 2017; Modena et al. 2015; Borri et al. 2011; Cancelliere et al. 2010; Oliveira et al. 2010). The great diversity of ages, environments and materials used to construct arches impose a significant burden on generalizing material properties and thus the reliability and predictability of strengthening is isolated to the reliability of the material properties.

The analysis of unreinforced masonry arches has focused on determining the limiting mechanism and their retrofitting has focused on maximizing strength. While this duality is understandable and expected, it overlooks what exists in-between those limits. The limiting mechanism of an unreinforced arch has a capacity that at best approaches one-tenth of the material capacity and capitalizing on this difference has been theoretically introduced (Stockdale 2016; Heyman 1966). A notable consequence of reinforcing the minimum mechanism is the introduction new mechanisms and thus the need to look beyond the minimum arises. This need drove the creation of a first-order assessment strategy and the Kinematic Collapse Load Calculator (KCLC) (Stockdale and Milani 2018a; Stockdale et al. 2018). The KCLC is an interactive open source tool designed to analyse the mechanized failure of masonry arches. It utilizes ideal conditions of masonry and the closed form solutions of a simple limit analysis approach that produces collapse and reaction values based on user defined hinge and loading configurations. In its current form the KCLC is limited to education, but the simple structure of the interface and the underlying LA approach were designed to adapt and expand. One adaptation to the LA model has been the incorporation of any drawn arch geometry through a CAD based data extraction technique (Stockdale and Milani 2018b). Adapting this technique into the KCLC removes many of the ideal geometric conditions. Now the ideal behaviours need to expand and adapt to real conditions through experimentation.

The first experimental tests measuring the seismic capacities of a family of admissible mechanisms for an arch through a tilting plane has been executed (Stockdale, Sarhosis and Milani 2018). The initial assessment of the experimental results revealed that the general behaviour of the arch was captured by the LA model, but that the capacity was significantly overestimated for the majority of the tested hinge configurations. Additionally, the observed failure of the arch was not limited to the traditional four-hinged mechanism for all 82 recorded collapses, but rather a three-hinge plus one slip-joint mechanism controlled the failure for certain configurations.

The KCLC was developed directly from and for the structural design and analysis of masonry arches through the examination of kinematically admissible mechanisms. The first experimental campaign into the seismic capacity of a family of kinematically admissible mechanisms for a dry-stack masonry arch revealed non-ideal conditions and capacities while maintaining the expected behaviour of the system. It is now necessary to adapt the KCLC to match the experimentation and observations, but they themselves must also be justified as they are not ideal. This work simultaneously addresses both issues and utilizes them to establish a novel analysis platform for designing and defining the failure and seismic capacity of masonry arches. First, in Section 2, the tilting plane analysis and six additional mechanism types arising from the consideration of a slip joint at the base hinge are defined and incorporated into KCLC and the LA model through modifications to the equilibrium conditions. Section 3 then describes the experimental setup. Section 4 presents the LA and DEM arch analysis models. The procedure, data and results are described in Section 5, and is followed by the post-processing and validation in Section 6. Utilizing the validation of the experimentation with the additional mechanism types, Section 7 presents the application of the limiting mechanism condition to the ideal parameters of the experiment and reveals potential sensitivities between reinforcement and capacity. This limiting condition is also expanded to non-circular arches through the incorporation of the CAD based data extraction. Finally, the violation of the non-stable kinematically admissible mechanism that arises from the flexural reinforcement of hinge joints and the traditional consideration of the thrust line is addressed in Section 8 to define reinforcement requirements for post-minimum mechanisms. The work is then concluded in Section 9.

2 KCLC, Tilting Plane and Mechanism Analysis

The original KCLC is an open source educational tool to expand the accessibility and understanding of masonry arch analysis, and to act as the foundation for a robust, efficient and effective structural analysis platform (Stockdale et al. 2018). In order for the transformation from purely educational to a professional application to occur, the approach must be able to model real conditions observed through experimentation. For the static testing of seismic

capacity, tilt table testing provides a cheap and efficient method of experimental analysis. To capitalize on this testing method, the KCLC must be adapted to account for the gravity decomposition.

Additionally, the first experimental campaign focusing on kinematic admissibility revealed a second admissible mechanism type (Stockdale, Sarhosis and Milani 2018). The traditional mechanism involves the development of four rotational hinges that alternate between the intrados and extrados (see Fig. 1). This second mechanism resulted in the release of the translational degree of freedom associated with the loss of static friction at the base hinge joint H_1, also shown in Fig. 1. Coupling the experimental results with the violation of the ideal no-slip condition revealed five additional plausible mechanism types to evaluate. These mechanisms range from Type I to Type VII. Type I represents the standard four-hinges mechanism. Type II, III and VI make up a group that replace rotations with slip translations. Type V, VI and VII establish a second group that remove a hinge from the evaluation by combining the release of slip and rotation at hinge H_1. This section presents the modified equilibrium equations for the gravity decomposition problem and the additional mechanism types, and their incorporation into the updated KCLC software developed in this work.

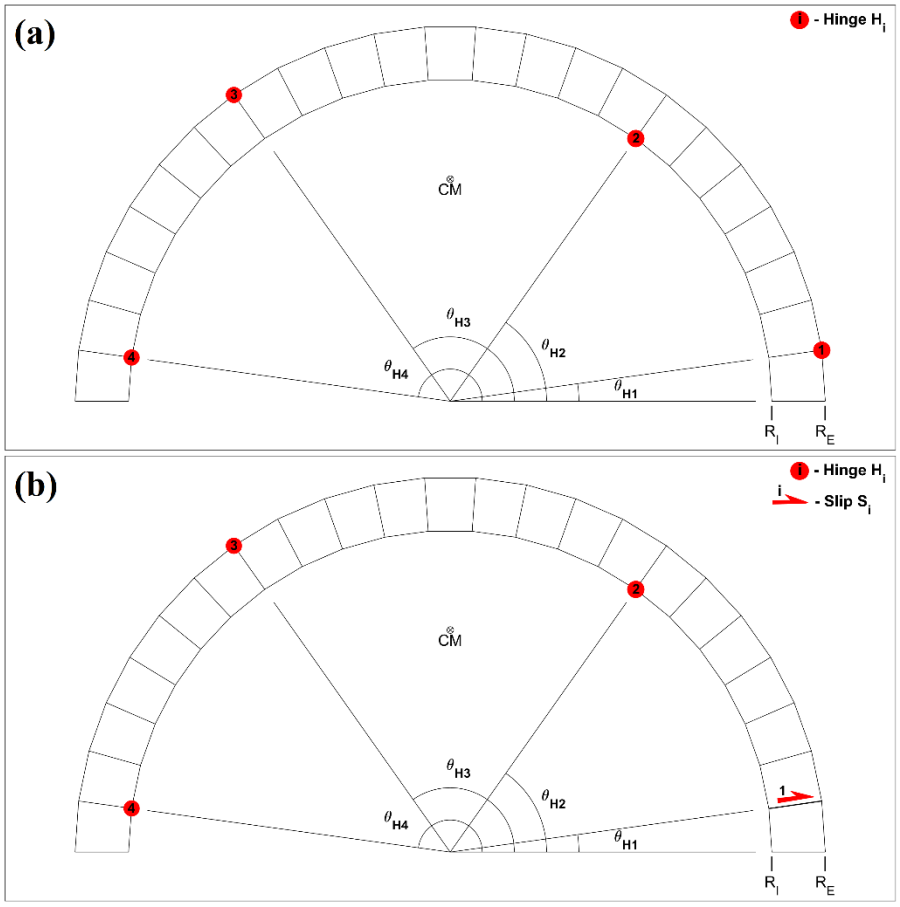

Fig. 1 Admissible mechanism configurations for the (a) standard four-hinged arch and a (b) three-hinge one-slip arch with hinge H_1 replaced with an outward slip S_1

2.1 KCLC Overview

The KCLC utilizes an equilibrium approach to the upper bound theorem of limit analysis and evaluates the collapse condition for a user defined geometry-hinge-load combination. The collapse multiplier is incorporated into the equilibrium equations as a reaction to balance equations and unknowns. The system is represented in matrix form as:

$$[BC]\{r\} = \{q\} \tag{1}$$

where ***BC*** is the balance matrix, ***r*** is the reaction vector, and ***q*** is the constants vector. From (1), the reaction vector is solved by:

$$\{r\} = [BC]^{-1}\{q\} \tag{2}$$

The equilibrium set is updated and evaluated with each hinge adjustment or geometry-loading modification. After evaluating the reaction vector, the results are processed to determine admissibility. The admissibility requirements are that the collapse multiplier is positive, the reactions at the hinges are compressive, and the thrust line passes through the hinge points. If the reaction set is admissible, they are displayed, and the thrust line is plotted. Figure 2 shows the updated KCLC with an admissible and non-admissible condition for the original horizontal loading condition and the standard Type I mechanism (see Appendix A for the list of equilibrium equations).

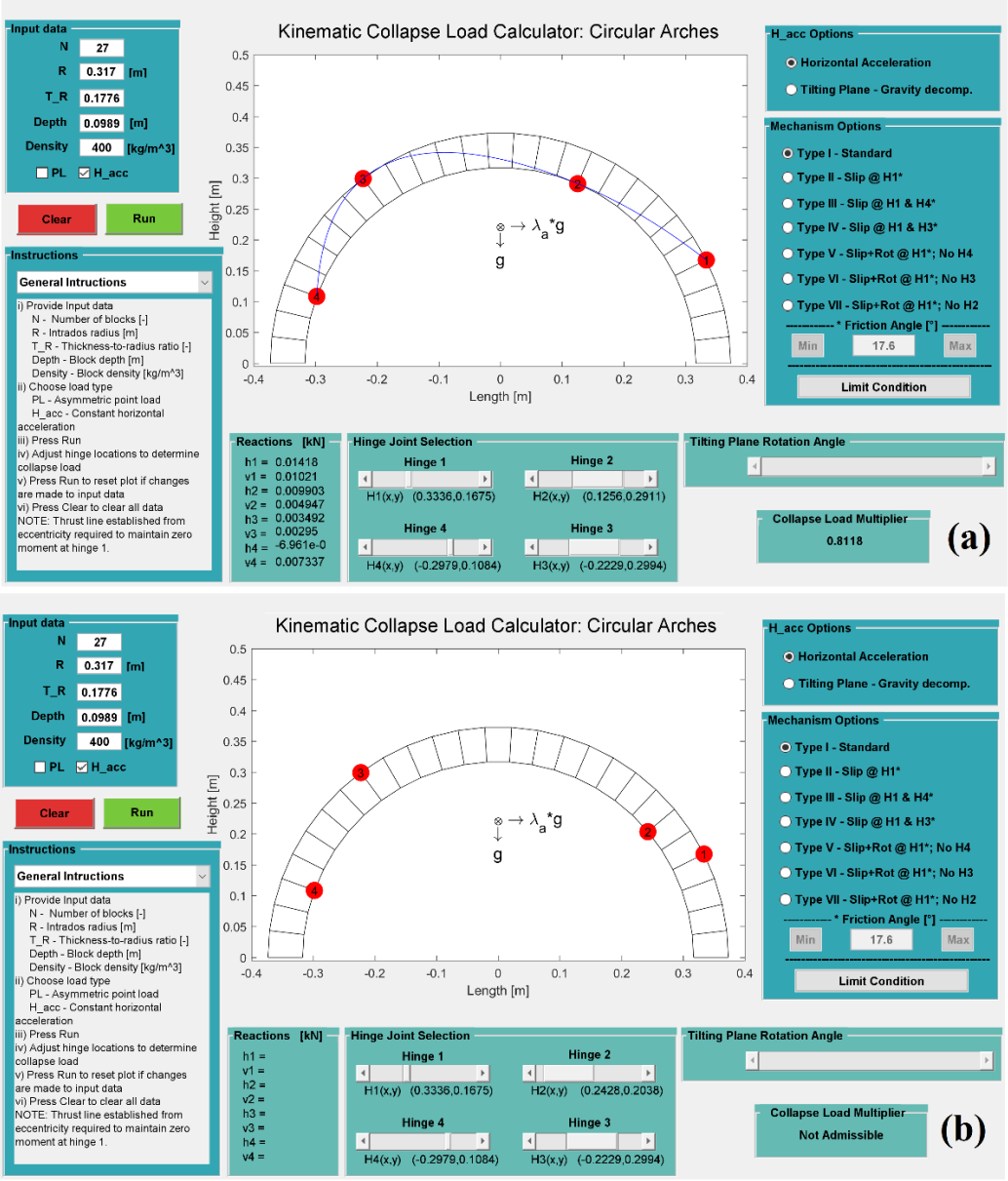

Fig. 2 An (a) admissible and (b) non-admissible hinge configuration for the standard Type I mechanism subjected to constant horizontal acceleration

2.2 Tilting Plane and Type I Mechanism

Figure 3 shows the equilibrium condition for the standard Type I mechanism. From Figure 3, the collapse load multiplier for the asymmetric point load condition, λ_P, is set to zero when evaluating the horizontal acceleration collapse multiplier, λ_a, and vice versa. The collapse multiplier λ_a is determined as a percentage of gravity, and its

inclusion increases the net acceleration experienced by the arch. A tilting plane however maintains a constant acceleration that is decomposed into vertical and horizontal components. Maintaining the collapse multiplier as a percentage of gravity, the tilting plane problem is addressed by decomposing the vertical acceleration, v_{acc}, and horizontal acceleration, h_{acc}, into

$$v_{acc} = -g \cdot \sin(\theta_t) \tag{3}$$

and

$$h_{acc} = g \cdot (\lambda_a + \cos(\theta_t)) \tag{4}$$

respectively (see Fig. 3). The maximum rotation angle is then obtained by determining the tilting plane rotation angle, θ_t, that results in a collapse multiplier equal to zero.

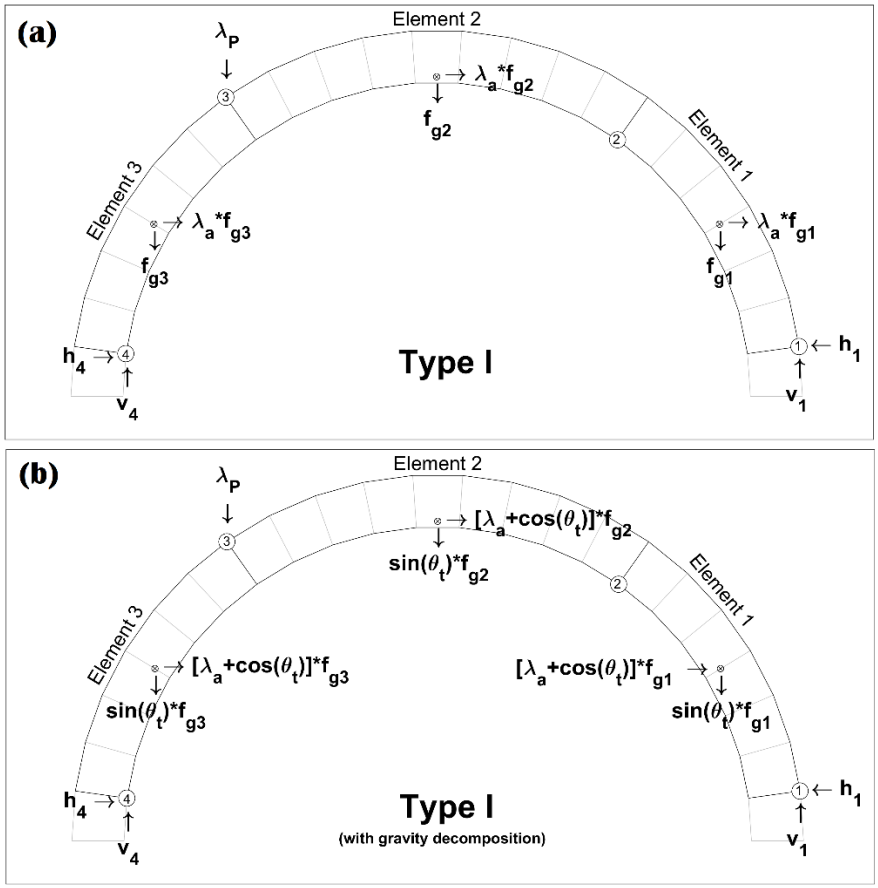

Fig. 3 Equilibrium condition for the standard Type I mechanism (a) without and (b) with the inclusion of gravity decomposition associated with a tilting plane

The incorporation of the tilting plane into the KCLC is through the manual adjustment of the rotation angle as can be seen in Fig. 4. Note that the exceedance of the maximum rotation angle produces a non-admissible condition.

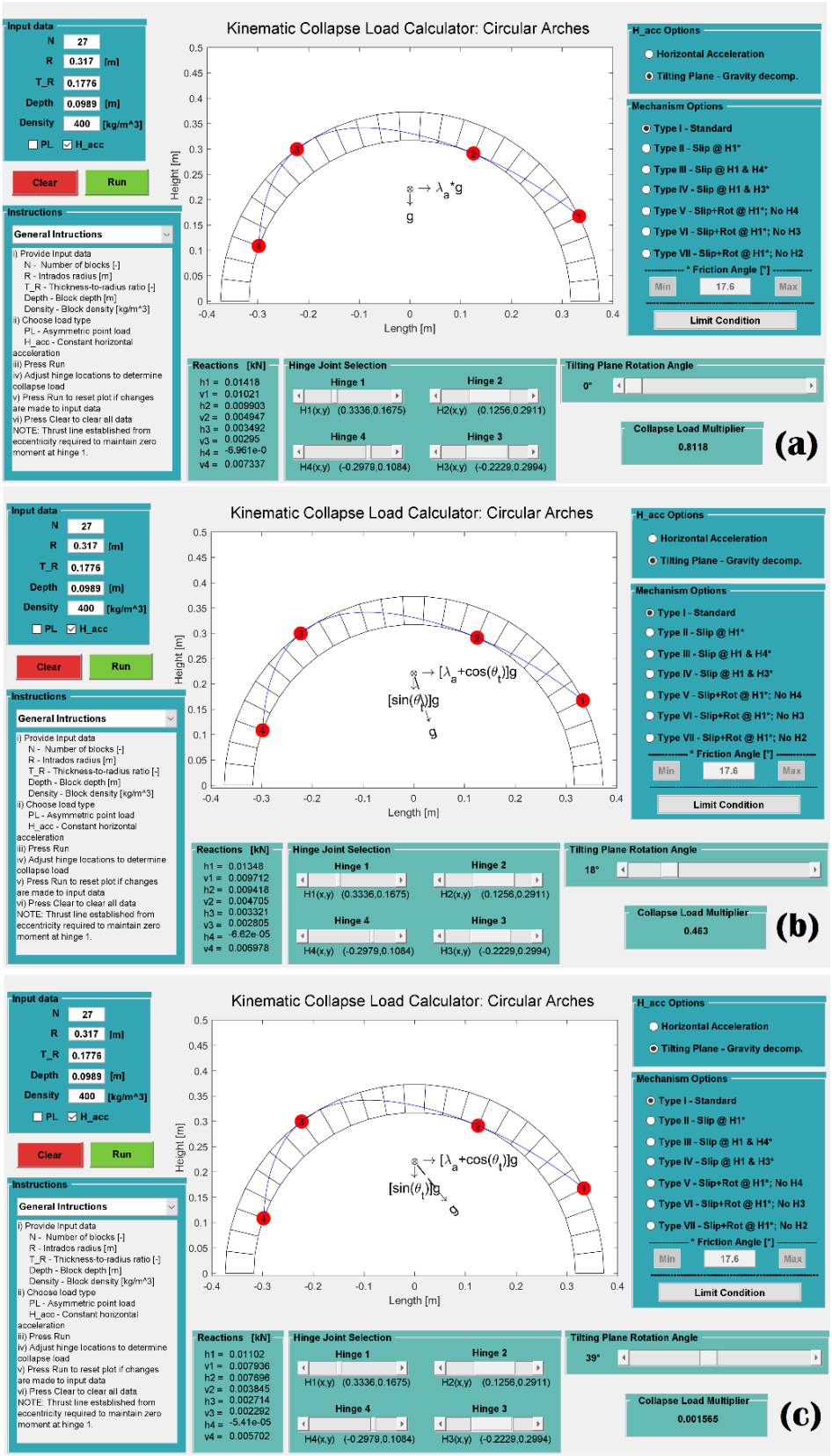

Fig. 4 Tilting plane limit analysis of a masonry arch with the standard Type I mechanism at the (a) beginning of rotation, an (b) intermittent rotation, and the (c) maximum rotation angle.

2.3 Slip Replacement Mechanisms – Type II, III & IV

Figure 5 shows the equilibrium condition for the mechanisms Type II through Type IV which are based on the replacement of hinge H_1 with a slip translation S_1. Mechanism Type II represents the experimentally observed condition of only the H_1 to S_1 exchange. Type III and Type IV mechanisms combine the exchange of H_4 to S_4 and H_3 to S_3 respectively with the H_1-S_1 switch.

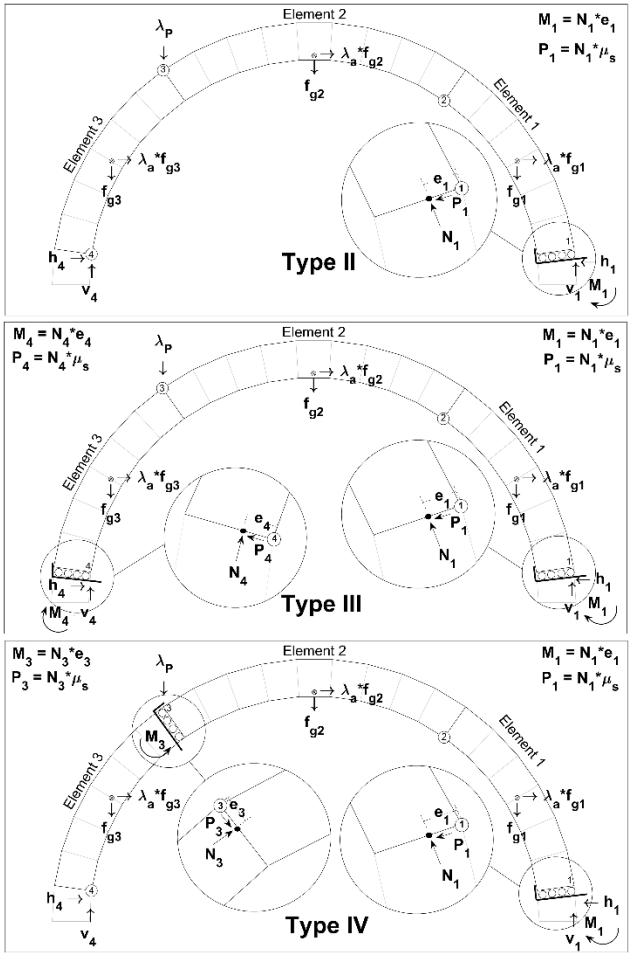

Fig. 5 Equilibrium conditions for the Type II, III and IV mechanisms

The exchange of rotation to slip at a joint has the consequence of removing the singularity of the thrust line boundary condition at that joint. Rotations fix the thrust line at the hinge, but the slip condition releases that restraint. Without the knowledge of the thrust line location at the slip joint, a moment must be included into the equilibrium condition. This moment is defined as

$$M_i = e_i \cdot N_i \tag{5}$$

for the i[th] mechanical joint. The eccentricity, e_i , is taken as the distance from the standard hinge location and the reaction force, N_i, is the normal force to the mechanical joint. The inclusion of the moment into the reaction variables is then balanced by the static friction relationship

$$P_i = N_i \cdot \mu_S \tag{6}$$

and

$$\theta_S = \tan^{-1}(\mu_S) \tag{7}$$

where P_i is the parallel reaction force at the i[th] joint, μ_S is the coefficient of static friction and θ_S is the friction angle. In terms of cartesian coordinates, the relationship between the horizontal and vertical reactions becomes

$$v_i = h_i \tan(\alpha_i) \tag{8}$$

where α_i is established through the reaction vector condition and the mechanical joint angle. For slip joints S_1, S_3 and S_4 the geometric relationships between the joint angle, the friction angle and the reaction vectors are shown in Fig. 6. Equation 8 provides the addition to **BC** necessary to balance the inclusion of M_i to **r**. Appendix A lists the developed equilibrium equations.

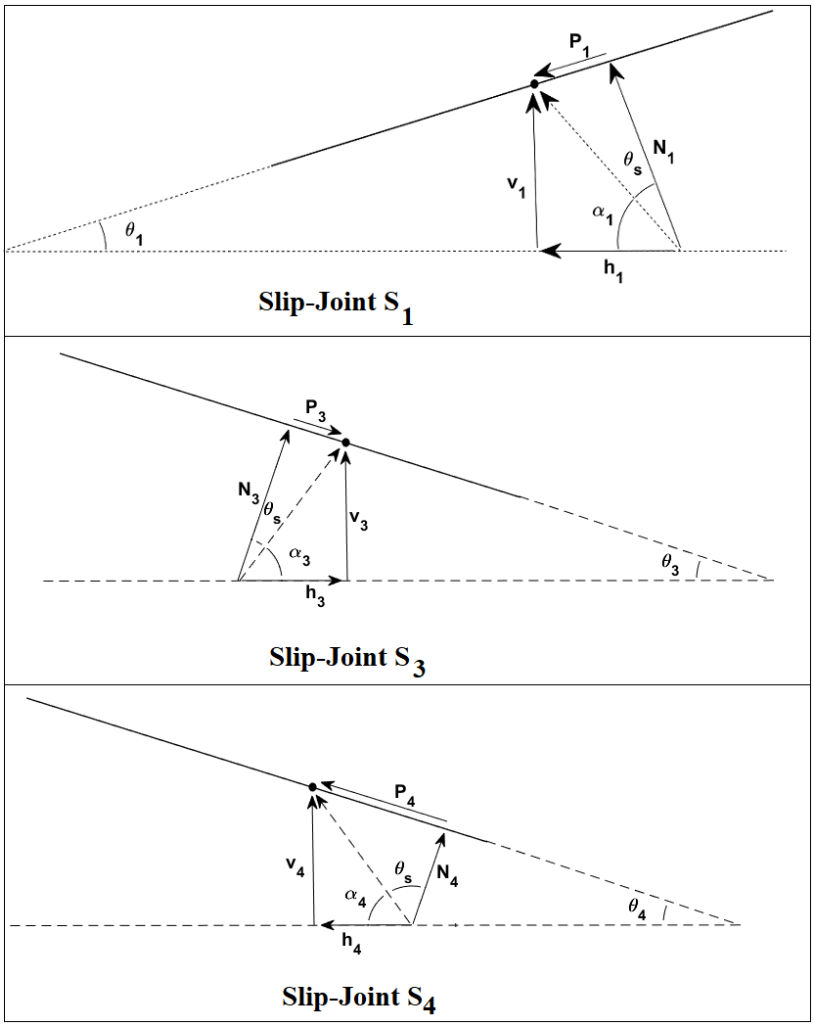

Fig. 6 Geometric relationships between the joint angle, friction angle, and reaction vectors for the three slip joints used in the slip replacement mechanisms.

In the context of admissibility, the trust line must cross the joint boundary in such a way that the nature of the mechanism under evaluation is maintained. Additionally, a negative eccentricity would indicate that the thrust line lies outside the mechanical joint boundary. This limits the eccentricity between the hinge edge and half the joint thickness

$$0 \leq e_i \leq \frac{1}{2}t \tag{9}$$

2.3.1 Mechanism Type II

The Type II mechanism exchanges H_1 for S_1. For Eqn. 8

$$\alpha_1 = \frac{\pi}{2} - \theta_1 - \theta_S \tag{10}$$

and it is established from the geometric relationship seen in Fig. 6.

Figure 7 shows a Type II mechanism with two different friction angles that produce an admissible mechanism for the given mechanical joint configuration.

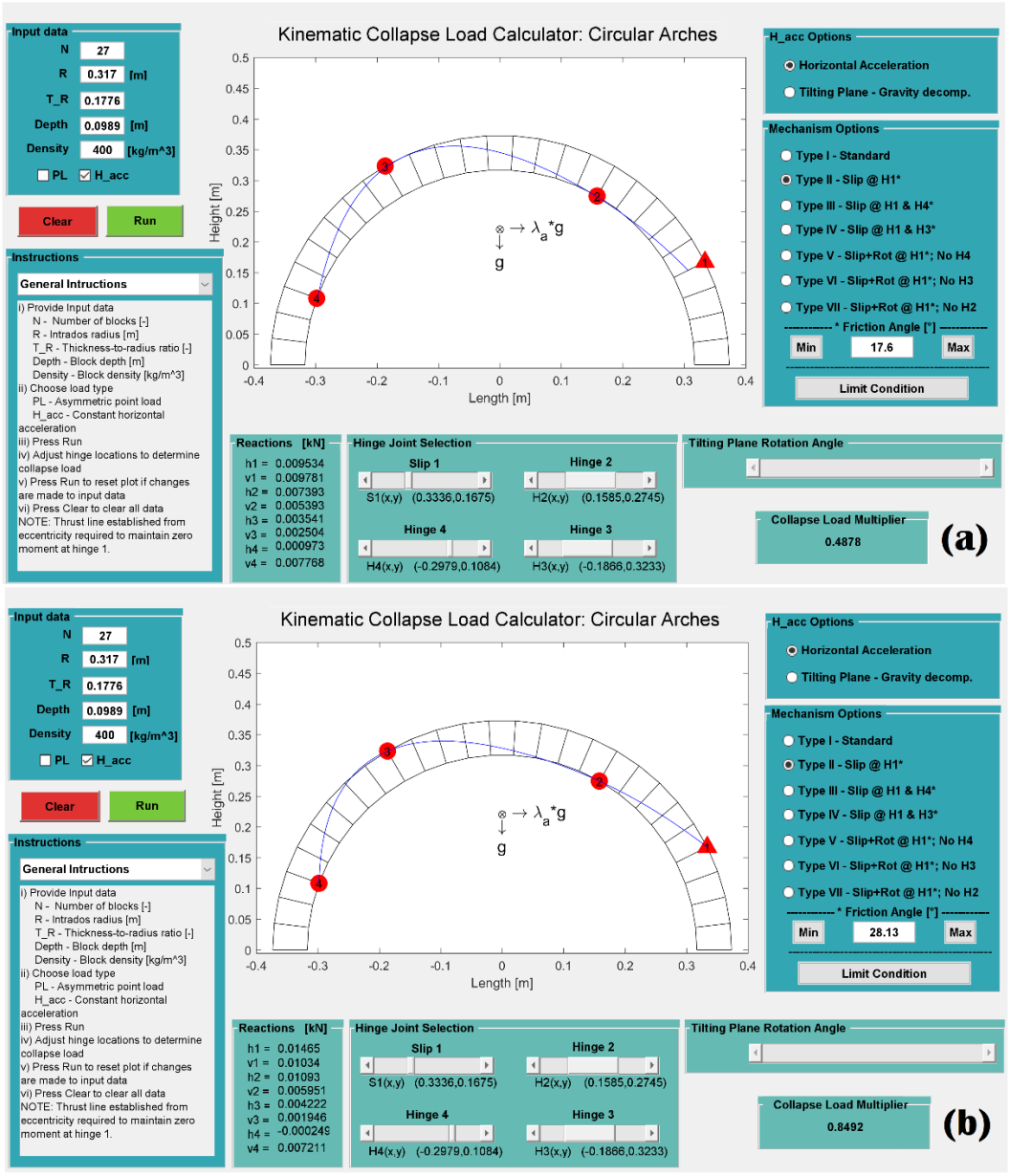

Fig. 7 Admissible Type II mechanism under constant horizontal acceleration with friction angles of (a) 17.6° and (b) 28.13°

2.3.2 Mechanism Type III

The Type III mechanism exchanges H_4 for S_4 in addition to the H_1-S_1 switch. This results in another use of Eqn. 8 with

$$\alpha_4 = \frac{3\pi}{2} - \theta_4 - \theta_S \tag{11}$$

as established from the geometric relationship seen in Fig. 6.

Figure 8 shows a Type III mechanism with two friction angles that produce an admissible mechanism for the given mechanical joint configuration.

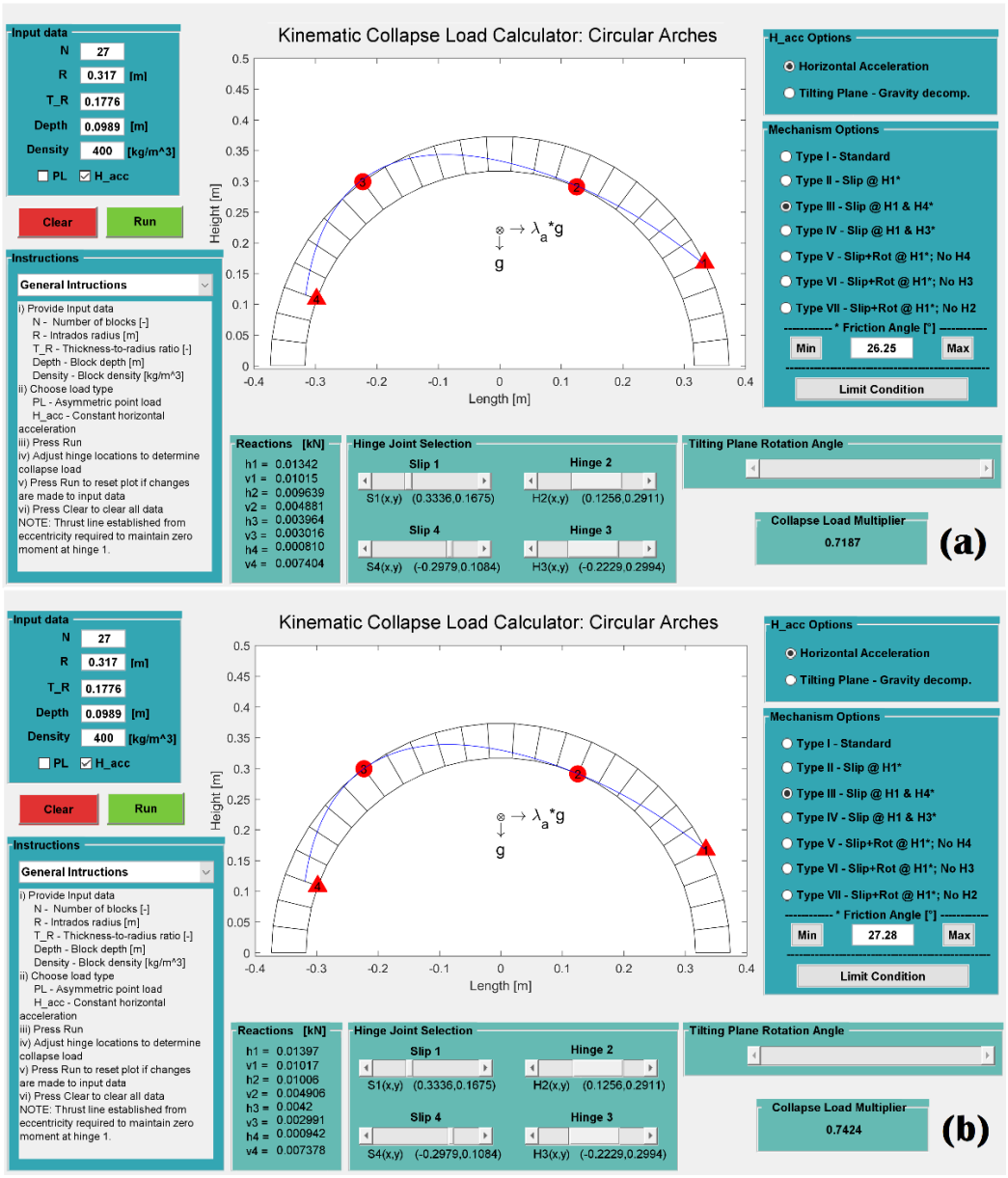

Fig. 8 Admissible Type III mechanism under constant horizontal acceleration with friction angles of (a) 26.25° and (b) 27.28°

2.3.3 Mechanism Type IV

The Type IV mechanism exchanges H_3 for S_3 in addition to the H_1-S_1 switch. This also results in another addition of Eqn. 8 with

$$\alpha_3 = \frac{\pi}{2} - \theta_3 - \theta_S \tag{12}$$

as established from the geometric relationship shown in Fig. 6.

Figure 9 shows a Type IV mechanism with two friction angles that produce an admissible mechanism for the given mechanical joint configuration.

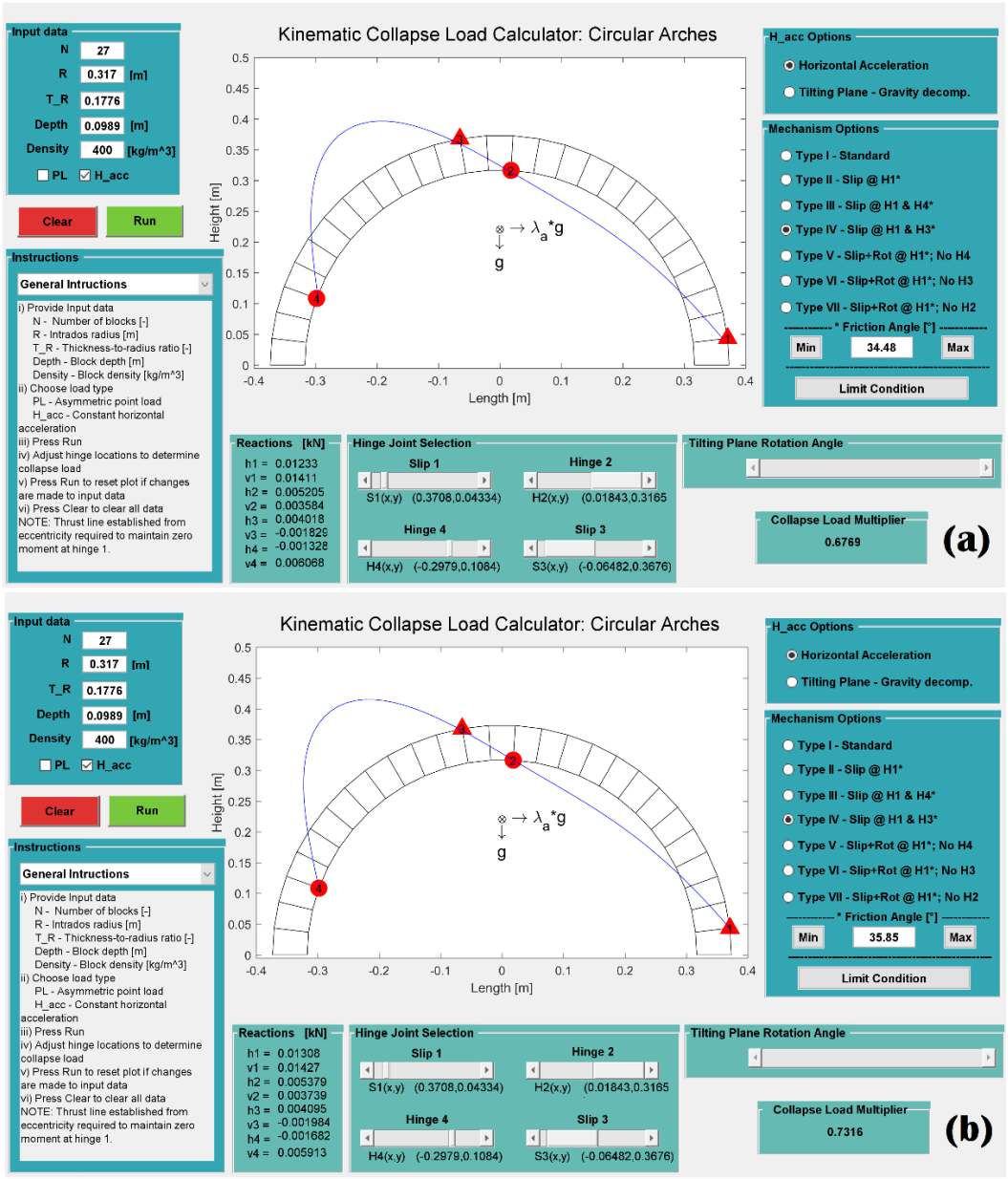

Fig. 9 Admissible Type IV mechanism under constant horizontal acceleration with friction angles of (a) 34.48° and (b) 35.85°

2.4 Reduced Hinge Mechanisms – Type V, VI & VII

Figure 10 shows the equilibrium conditions for mechanisms Type V, VI and VII. Each mechanism is developed from the condition of a double release of freedom (slip and rotation) at H_1 in exchange for one of the other hinges. For each condition, the removal of a hinge results in a three pinned arch. Therefore, the inclusion of the friction condition (i.e. Eqns. 8 and 9) at H_1 is required to balance the collapse multiplier. The inclusion of a moment is unnecessary as the hinge defines the thrust line location. The equilibrium equations are presented in Appendix A.

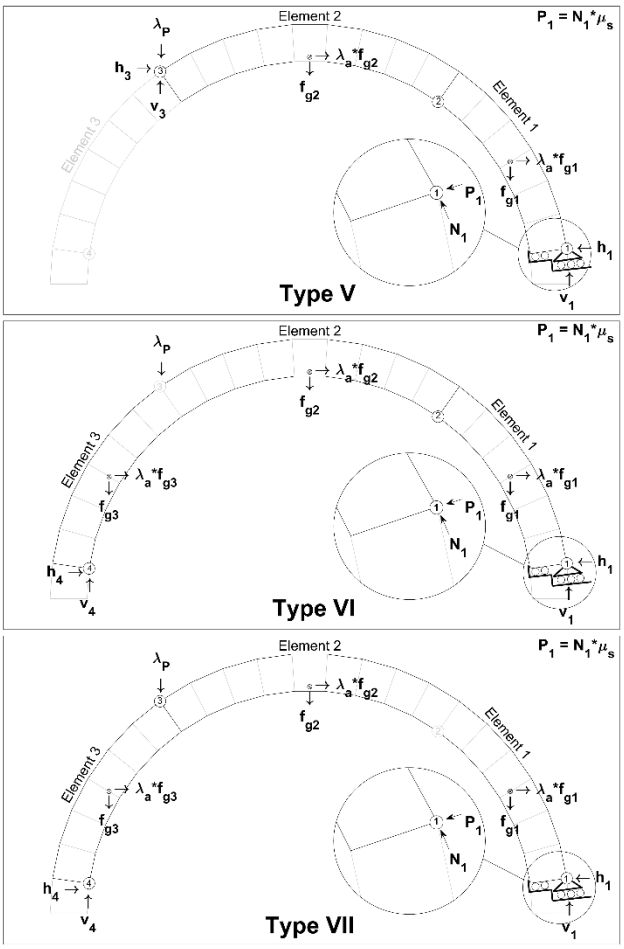

Fig. 10 Equilibrium conditions for the Type V, VI and VII mechanisms

2.4.1 Mechanism Type V

Mechanism Type V removes H_4 and thus element 3 from the system. Figure 11 shows a Type V mechanism with two friction angles that produce an admissible mechanism for the given mechanical joint configuration.

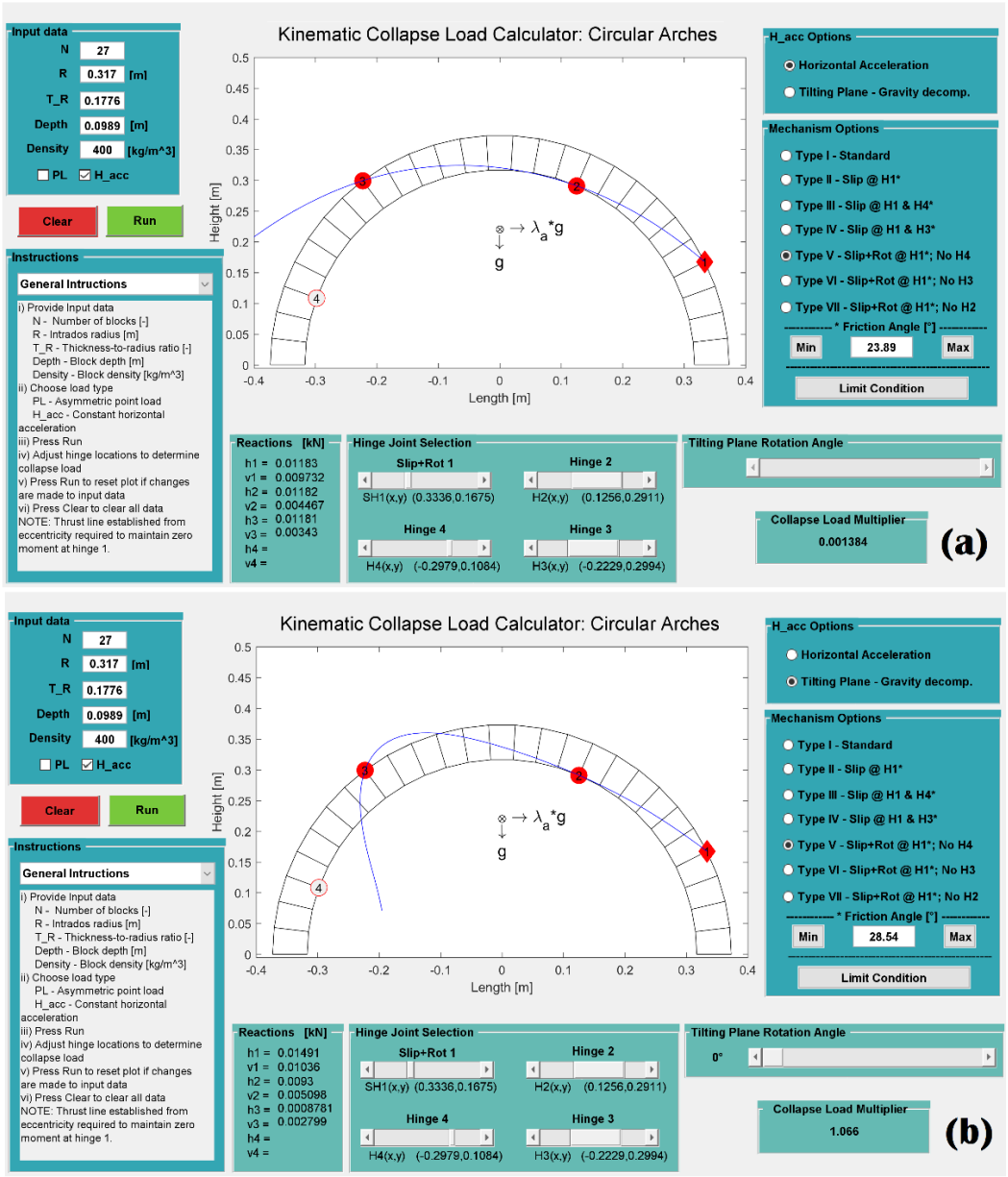

Fig. 11 Admissible Type V mechanism under constant horizontal acceleration with friction angles of (a) 23.89° and (b) 28.54°

2.4.2 Mechanism Type VI

Mechanism Type VI removes H_3 and thus combines element 2 and 3 into a single rigid element. Figure 12 shows a Type VI mechanism with two friction angles that produce an admissible mechanism for the given mechanical joint configuration.

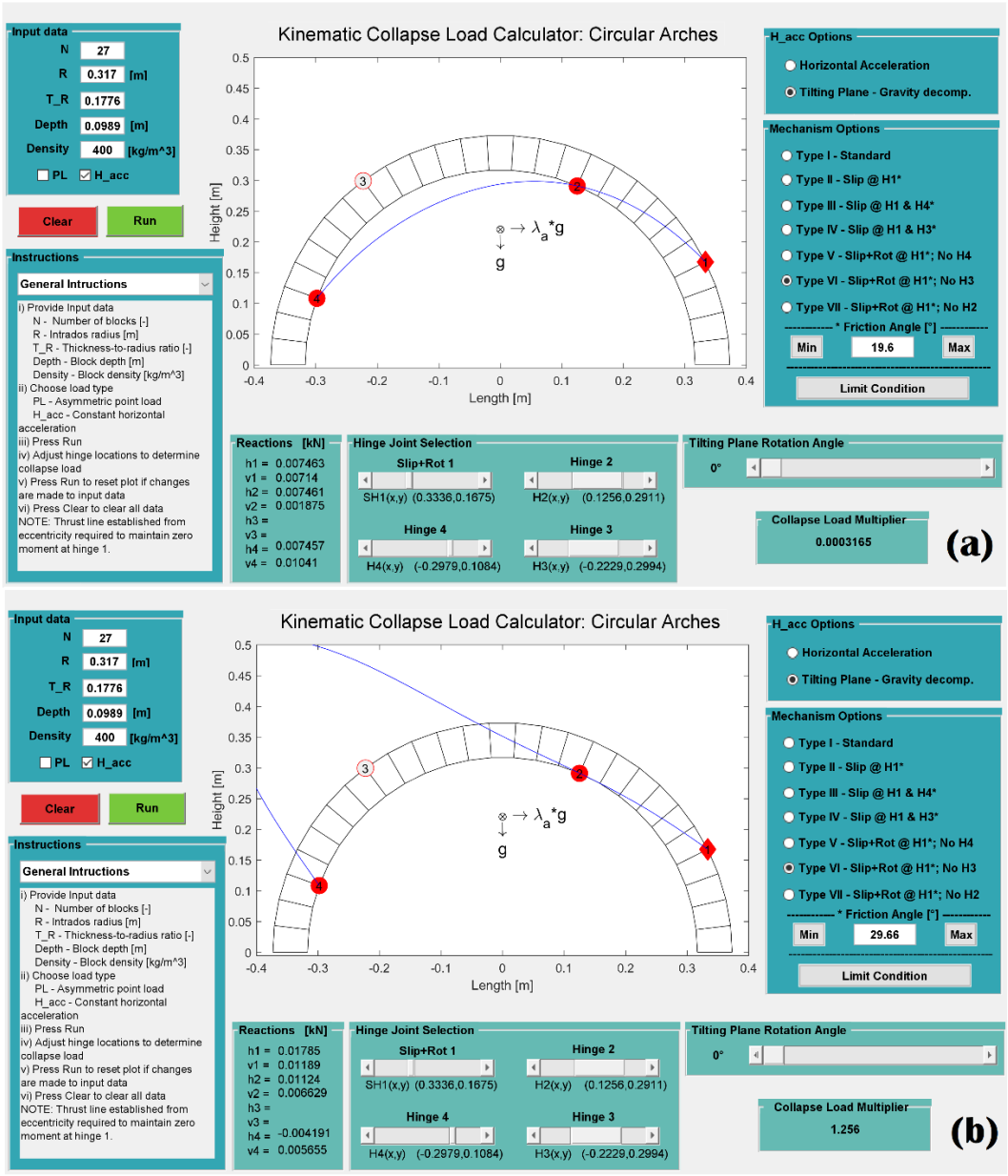

Fig. 12 Admissible Type VI mechanism under constant horizontal acceleration with friction angles of (a) 19.6° and (b) 29.66°

2.4.3 Mechanism Type VII

Mechanism Type VII removes H_2 and thus combines element 1 and 2 into a single rigid element. Figure 13 shows a Type VII mechanism with two friction angles that produce an admissible mechanism for the given mechanical joint configuration.

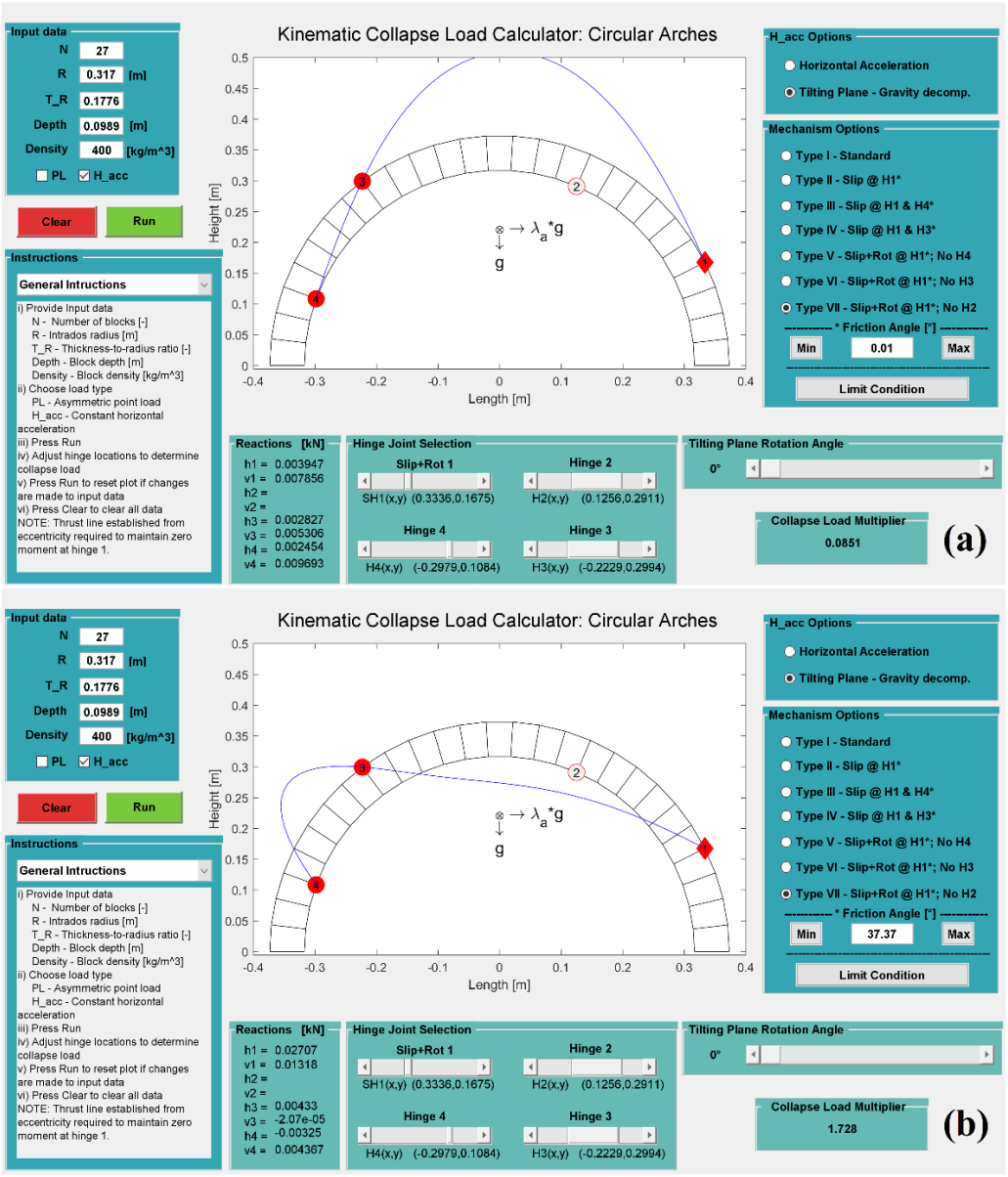

Fig. 13 Admissible Type VII mechanism under constant horizontal acceleration with friction angles of (a) 0.01° and (b) 37.37°

3 Experimental Setup

As expressed in the introduction, the objective of this work is to further the development of a simple and robust structural analysis tool for the seismic assessment of masonry arches through the adaptation of the LA model based on experimental behaviour. For seismic capacity, quasi-static tilting plane tests provide an efficient and effective method to examine the effects of horizontal accelerations and can be used to establish base values that are ultimately adjusted through correction factors to account for non-linear dynamic behaviours. This section presents the first experimental campaign combining tilting plane testing with the control of the mechanical joints (Stockdale, Sarhosis and Milani 2018).

A 27-block semi-circular arch was chosen for the experiment. The block count was selected such that there were many options of admissible configurations. The two base blocks were fixed to the platform and variations of five joints for both hinges H_1 and H_4 were selected. Taking the minimum mechanism for each H_1-H_4 pairs produced 25 distinct mechanisms to evaluate.

3.1 Arch Construction

Timber was chosen to construct the blocks to ensure they were durable enough to obtain a minimum of 75 collapses to measure the 25 mechanisms at least three times each. Three 47mm x 75mm Canadian Lumber Standard timber boards were combined to construct the blocks. Both 75mm sides of one board and one 75mm side of the other boards were planed and then the boards were glued together on the planed sides. Each face of the combined boards was then planed to establish clean faces and sharp edges. This process increased the final block-depth to create a more stable arch with respect to the out-of-plane behaviour. The blocks were then cut from a trapezoid template with a short span of 38mm and tapered sides of 3.33° from square. The block faces that make the arch boundary joints were then scarified in an attempt to increase roughness.

After constructing the blocks, they were assembled and adjusted to establish the most stable configuration (see Fig. 14**)**. The blocks were numbered, oriented, and the exposed faces were painted white with a point grid applied across each joint. The point grid template is shown in Fig. 16. The mass, block dimensions and point grid lengths were recorded.

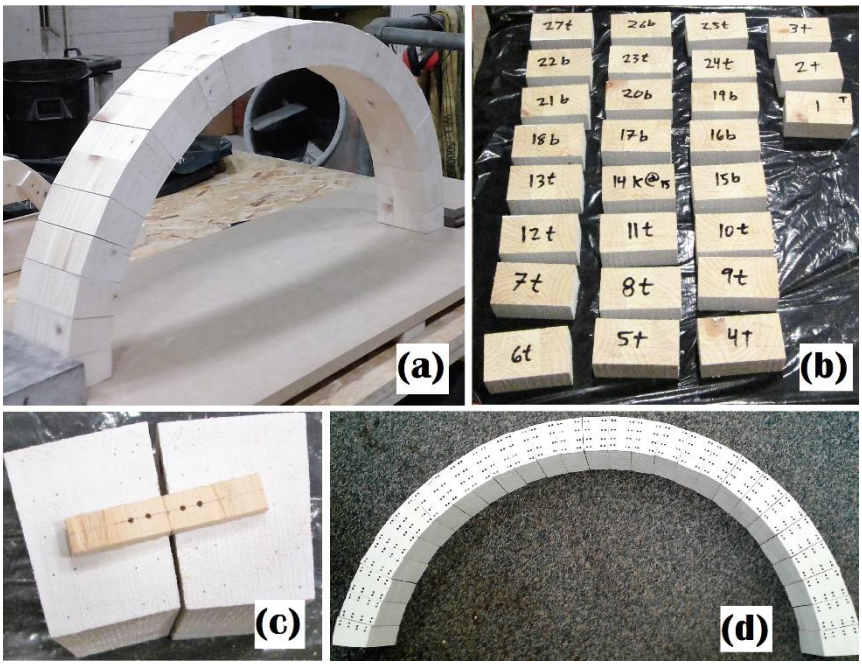

Fig. 14 Photographs of (a) the best fit configuration; the (b) number and orientation marking; the (c) point grid template; and (d) the final arch layout.

Figure 15 presents the constructed arch and the tilting platform. The final layout was established by anchoring the left base block to the platform and assembling the arch left to right. Shims were added to the extrados of the right base block to establish the most stable configuration prior to anchoring the second base block. The final arch measured a clear span of 0.6695±0.0005 m and a rise of 0.3170±0.0005 m. The platform was constructed from a dense composite board with risers. This allowed the use of the negative space for anchoring. The riser on the left in Fig. 17 was aligned perpendicular to the arch and spanned the width of the platform to define in-plane rotations. A threaded steel rod was attached with eyebolts parallel to the rotation edge and a lifting chain was attached to the bar at the centreline of the arch plane. Nuts and washers were added to the threaded bar to maintain the lifting chain at centreline.

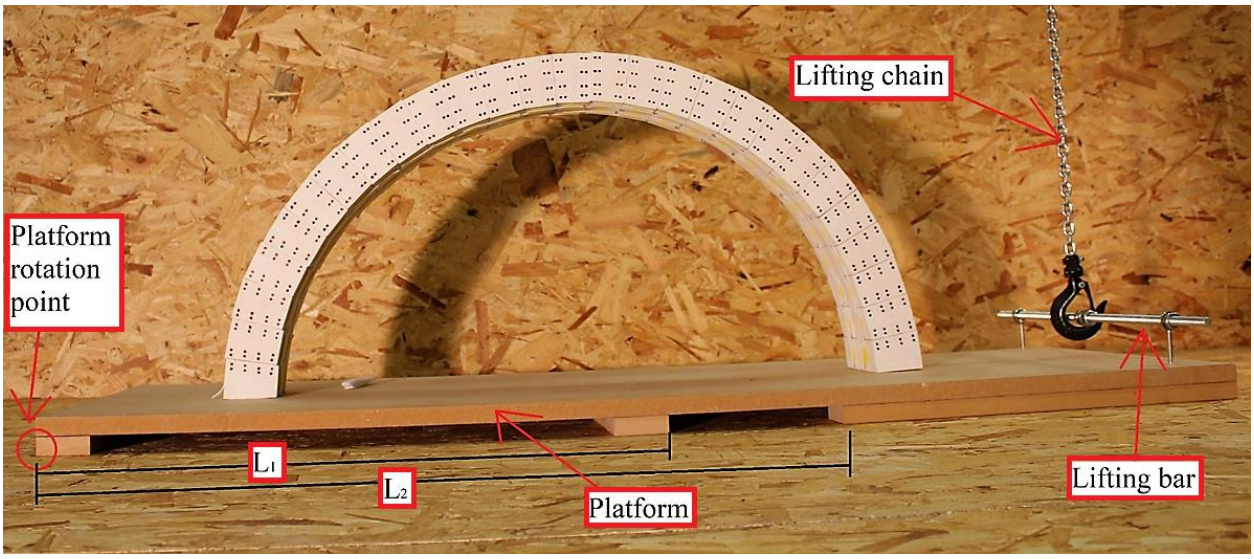

Fig. 15 Image and annotation of the 27-block arch experimental setup with L_1 and L_2 representing measured lengths parallel to the platform plane

3.1.1 Mechanical Joint Control

The mechanical joint control system was constructed with Velcro®. The lightweight of timber allowed the use of the shear strength of Velcro® to resist hinge rotations while its own lighter weight ensures a negligible effect to the stable system. Hook-sided tabs were adhered in sets of two to both the intrados and extrados of each block creating two parallel reinforcing planes as shown in Fig. 18. The mechanical joint control was then achieved through applying loop-sided straps across all non-mechanical joints (Fig 16).

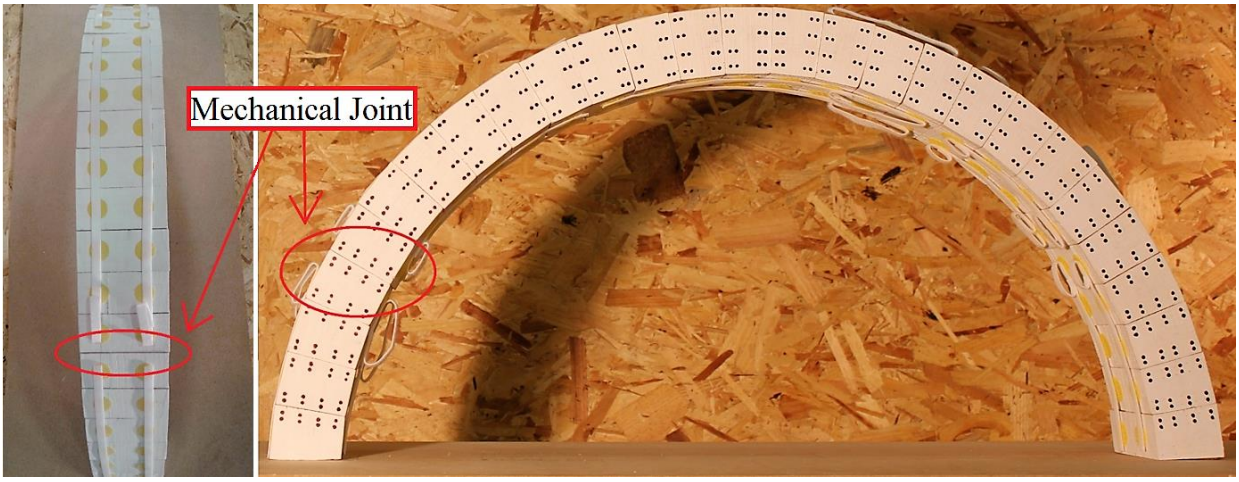

Fig. 16 Image and identification of a defined mechanical hinge joint

3.2 Tilting Table

The tilting table was used to introduce quasi-static horizontal accelerations. Gravity's constant direction and magnitude result in the rotation of acceleration being equal to the tilting plane's rotation. Therefore, determining the rotation angle is the only required information. The rotation of the tilting plane can be determined by

$$\theta_t = \sin^{-1}\frac{l}{L} \tag{13}$$

where l is the measured height after rotation of a known distance L along the plane of rotation (see Fig. 15). Section 5 presents the results of the experimental campaign executed with this constructed arch.

4 Arch Analysis Models

This section describes the development and verification of the geometric model, its incorporation into a custom KCLC and the DEM models developed in UDEC. The use of UDEC and its DEM approach was to establish a trifecta assessment for validation.

4.1 Geometric Model

The arch model was developed in AutoCAD®. As a result of the high sensitivity of the block angels that arise when constructing at this scale, a statistical approach was taken to establishing the model. To highlight this sensitivity, note that the difference between a 27-block and a 23-block arch with a thickness of 54 mm is a 0.5 mm change, or the width of a standard bandsaw blade, at either the intrados or extrados length. This sensitivity also carries onto the precision of the block measurements and results in a drawn arch that does not match the physical conditions. Although this sensitivity exists, the use of a single key to cut all of the blocks and the independent length measurements ensure that the construction and measurement errors of each block are independent and do not compound. Therefore, the block dimensions were averaged as shown in Fig. 19. The averaged block was drawn in AutoCAD® and the arch was constructed in the same manner as the real one, starting from the left to right. Then the intrados and extrados of random blocks were altered within the precision of the averaged block dimensions to fit the arch to the measured clear span, rise, and the slight rotation of the right base block that was shimmed. The drawn arch was then compared against the point cloud obtained from a lidar scan, and as can be seen in Fig 17 the two results are in good agreement. Figure 18 shows the final drawn arch and the nomenclature used to describe it, the experiment and the results.

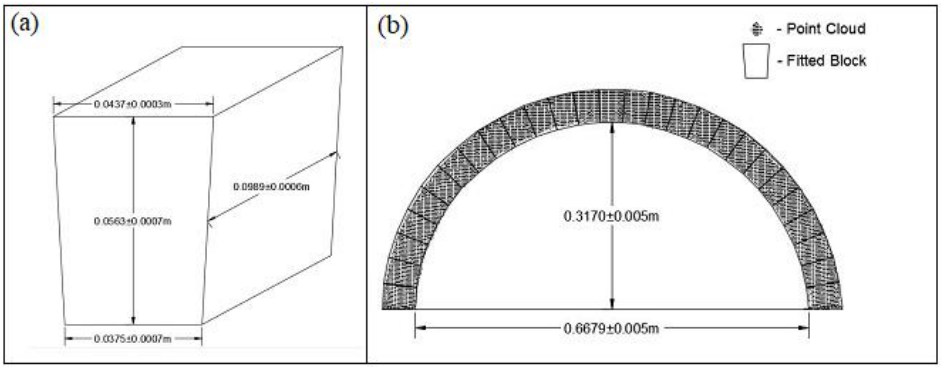

Fig. 17 The (a) averaged block dimensions and the (b) fitted block arch model

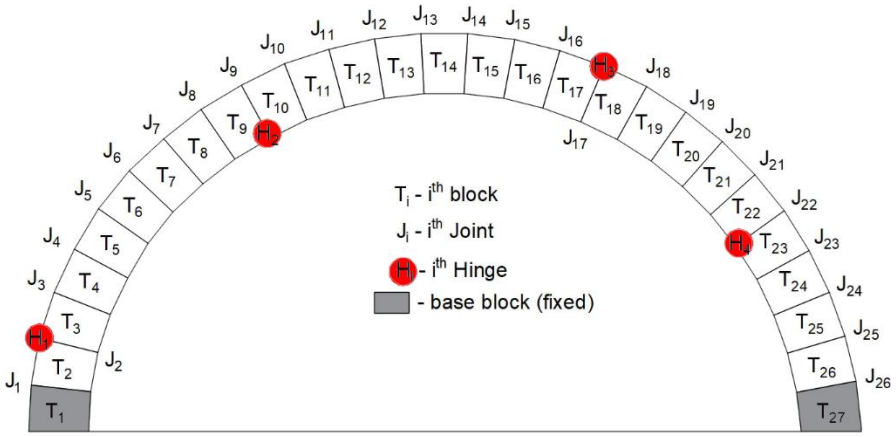

Fig. 18 Arch nomenclature

4.2 Limit Analysis Model

The LA model created for the experiment combines a simplified and custom KCLC with the drawn arch model and the recorded masses. The drawn arch model is incorporated through the application of a data extraction technique developed by Stockdale and Milani (2018b). This technique extracts the geometric data from the AutoCAD® drawn arch model and passes it to the customized KCLC. Figure 19 shows an image of the developed KCLC for the experimental arch. Note also that the recorded mass of each block was applied to the model and not averaged. This results in a small variation between the area and mass centroids as can be seen by the target and cross respectively in Fig. 19.

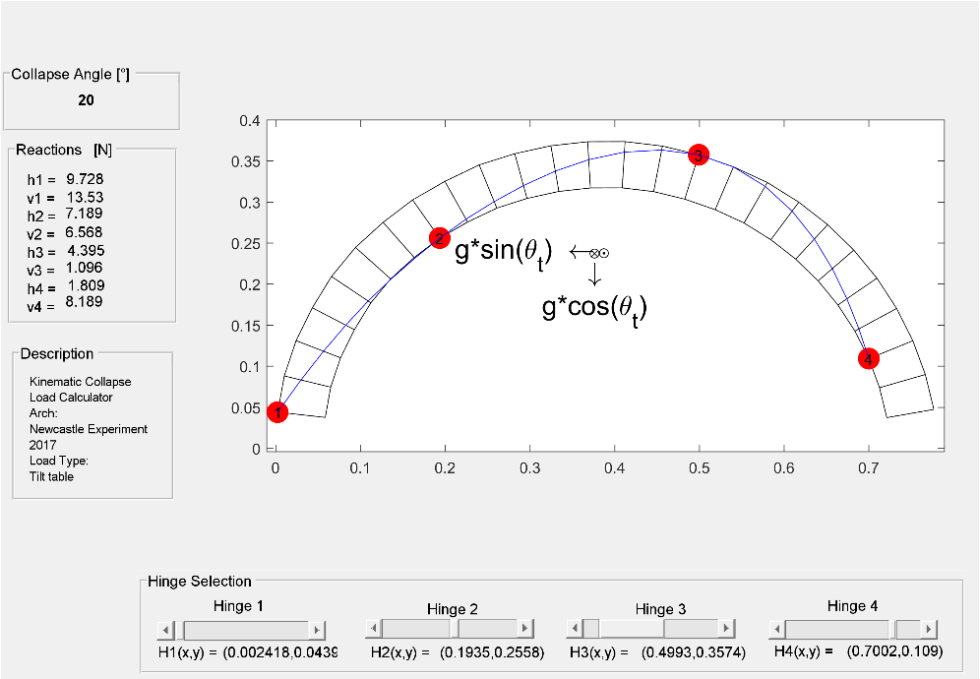

Fig. 19 Custom KCLC for the experimental arch subjected to a tilting plane

The hinges of the interactive model are then manually adjusted to the defined hinge sets to obtain the collapse angle.

4.3 Numerical analysis using the Discrete Element Method (DEM)

Interdependent geometric models were created to evaluate each of the 25 mechanical joint configurations of the experimental arch in the DEM model (see Fig 20). Voussoirs of the arch were represented by rigid blocks. The joints were represented as zero-thickness interface elements behaving according to the Coulomb failure criterion. Material properties assigned to the voussoirs of the arch ring are shown in Table 1. Material properties were obtained by small scale experimental testing of the individual voussoirs. The material parameter required to represent the behaviour of the rigid voussoirs is the unit weight (d), which was taken equal to 550 kg/m^3. Joints between voussoirs were presented by interfaces modelled using elastic-perfectly plastic coulomb slip joint area contact. For the joints, normal and shear stiffness were selected high so that no penetration between blocks was allowed to occur. The interface cohesive, tensile strength and the dilatation angle were set to zero; since in the experiment, the arch has been constructed using dry-joints. Self-weight effects were also included in the model as gravitational loads. Each analysis began by bringing the arch into a state of equilibrium under its own weight. Then, a tilting plane analysis was undertaken until the observed collapse of the arch (Figure 20b).

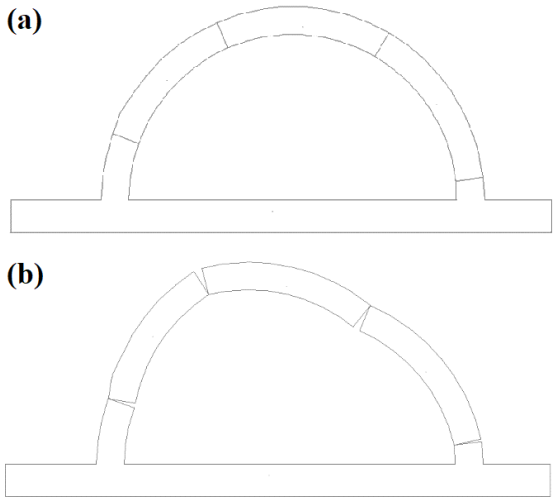

Fig. 20 Typical geometry (HS11) developed using the DEM mode (a) and failure observed failure mode (b)

Joint Normal Stiffness [GPa/m]	Joint Shear Stiffness [GPa/m]	Joint Friction Angle [°]	Joint Cohesive Strength [kPa]	Joint Tensile Strength [MPa]	Joint Dilation Angle [°]
20	10	22	0	0	0

Table 1 Material properties of the dry joints in the DEM model

5 Experimental Procedure, Data and Results

The experimental procedure included assembling the arch, setting the mechanical joint locations by applying the Velcro® loop straps, quasi-statically tilting the platform until collapse and measuring the heights l_1 and l_2 corresponding to the known platform lengths L_1 and L_2 respectively.

5.1 Hinge Sets

The experiment examined 25 unique mechanical joint configurations. The configuration sets were established through the use of the first-order assessment strategy developed by Stockdale and Milani (2018a). The 25 configurations are listed in Table 2.

Hinge Set	H_1	H_2	H_3	H_4	Hinge Set	H_1	H_2	H_3	H_4
1	J_1	J_8	J_{17}	J_{26}	**16**	J_4	J_{10}	J_{18}	J_{22}
2	J_1	J_8	J_{17}	J_{25}	**17**	J_4	J_{10}	J_{19}	J_{23}
3	J_1	J_8	J_{16}	J_{24}	**18**	J_4	J_{10}	J_{19}	J_{24}
4	J_1	J_8	J_{16}	J_{23}	**19**	J_4	J_{11}	J_{19}	J_{25}
5	J_1	J_8	J_{16}	J_{22}	**20**	J_4	J_{11}	J_{19}	J_{26}
6	J_2	J_8	J_{17}	J_{22}	**21**	J_5	J_{12}	J_{20}	J_{26}
7	J_2	J_9	J_{17}	J_{23}	**22**	J_5	J_{11}	J_{20}	J_{25}
8	J_2	J_9	J_{17}	J_{24}	**23**	J_5	J_{11}	J_{20}	J_{24}
9	J_2	J_9	J_{17}	J_{25}	**24**	J_5	J_{11}	J_{19}	J_{23}
10	J_2	J_9	J_{18}	J_{26}	**25**	J_5	J_{11}	J_{19}	J_{22}
11	J_3	J_{10}	J_{18}	J_{26}	Note: Refer to Fig. 20 for identifying joint location.				
12	J_3	J_{10}	J_{18}	J_{25}					
13	J_3	J_{10}	J_{17}	J_{24}					
14	J_3	J_9	J_{17}	J_{23}					
15	J_3	J_9	J_{18}	J_{22}					

Table 2 Hinge joint configurations for each tested hinge set

5.2 Collapse and Measurement

For each mechanical joint configuration set, a minimum of three collapses were executed. Each collapse was performed through the manual rotation of the platform through a lifting chain with a reverse locking hand crank (see Fig. 21). The chain was raised until the arch collapsed and at a rate that maintained a quasi-static acceleration state. At the point of collapse the crank was locked and the heights l_1 and l_2 were recorded. The platform was then lowered, and the system was reassembled. Each collapse was also recorded with a Cannon DSLR camera.

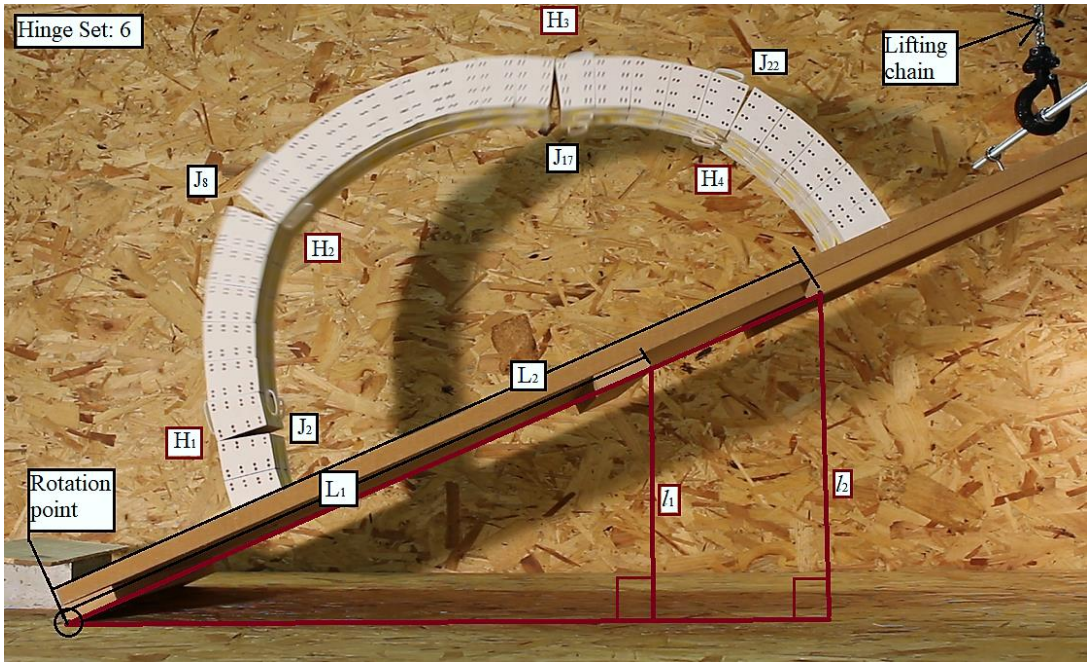

Fig. 21 Mechanical collapse and the associated measurement lengths

5.3 Data

The platform lengths L_1 and L_2 are 0.6110±0.0005 m and 0.7880±0.0005 m respectively. For each collapse, the heights and observed failure methods were recorded. The recorded values and observations are presented in Table B1 of Appendix B.

5.4 Results

The calculated rotation angles were obtained by first averaging the ratio of the height to platform length measurements for each run of a hinge set and then applying the result to Eqn. 13. The average and standard deviation of the rotation angle was then calculated for each hinge set. The measurement error was manually propagated due to the simplicity of the performed calculations and variables. Lastly, the propagated measurement error was compared against the standard deviation of the averaged rotation angles to establish the precision and identify its source. This evaluation revealed that the variance in the rotation angles controlled for all cases except hinge sets 20 and 21. Nonetheless, a minimum of two-digits of precision was obtained for all evaluated sets.

The collapse rotation angles from the experimentation, the LA model and the DEM analysis are presented in Fig. 22. The hinge sets are represented in a decision tree format with H_1 at the base. From Fig. 22 it can be seen that the capacity of the experimental arch can increase from the minimum mechanism's 16.7° rotation capacity to a maximum capacity of 30.3°. Therefore, reinforcing the arch with a flexural hinge reinforcement technique as shown in Fig. 23 will increase the capacity of the arch by a factor of 1.8. Also note that dominating factor controlling the capacity of the arch is the position of H_1 with the position of H_4 having a secondary effect. Additionally, both the LA model and DEM analysis captured the behaviour of the experimentation, but the LA model overestimated capacity on all counts and the DEM model for the upper three positions of H_1.

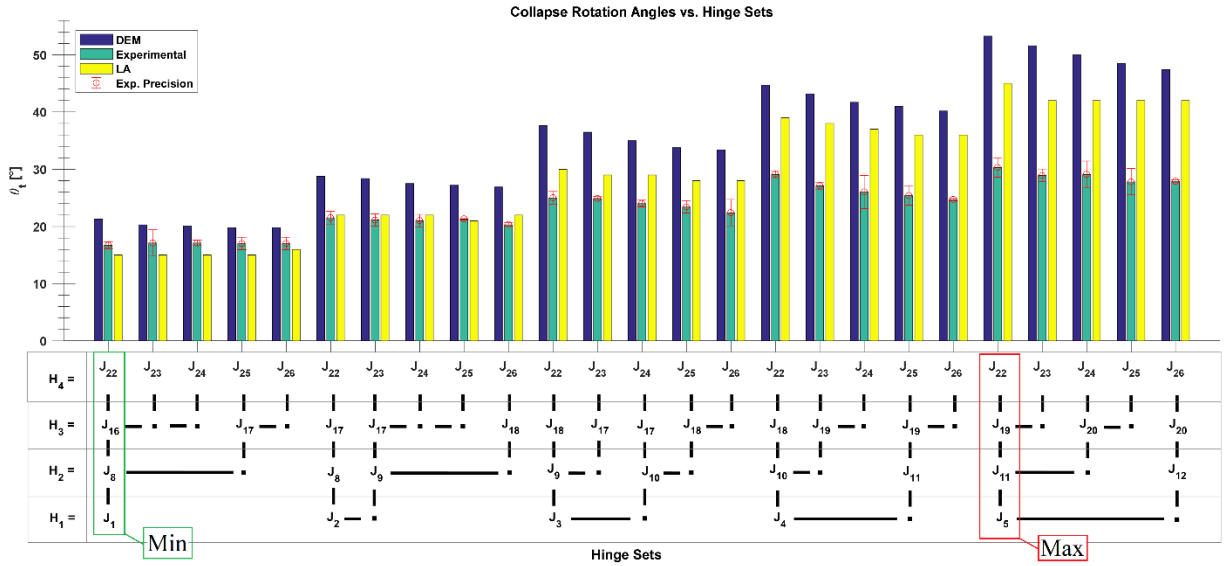

Fig. 22 Experimental, LA and DEM obtained collapse rotation angles versus hinge sets.

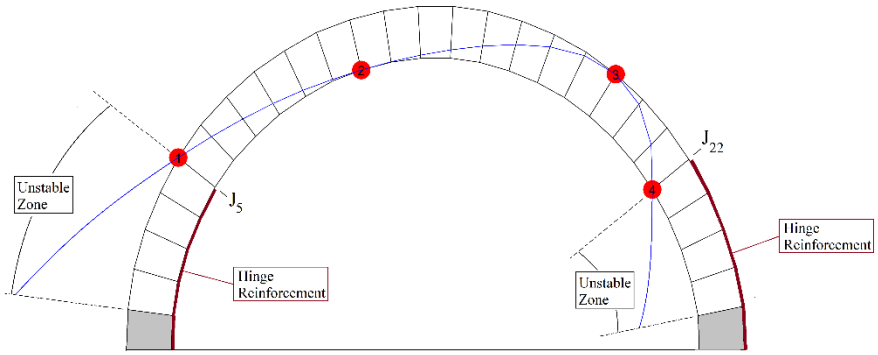

Fig. 23 Flexural hinge reinforcement layout to obtain the maximum capacity of the tested hinge sets.

The results of the analyses indicate that although the behaviour was captured, there exists some fundamental errors in the models that are resulting in significant overestimates when evaluated against the experimentation. To address this issue an examination of the recorded collapses was performed.

5.5 Experimental Observations

In addition to the length measurements taken for each collapse, a video recording was made. Review of these recordings revealed two non-ideal conditions in the experimentation. First, the Type II mechanism was clearly identified for all collapses with H_1 set at J_4 (see Fig. 23). Slip at H_1 did occur in previous collapses, but it was inconsistent and attributed to the non-perfect geometry and the 2D simplification. Additionally, base deformations developed through reinforced hinge rotations were observable at J_1 when H_1 was higher than J_3 as can also be seen in Fig. 24.

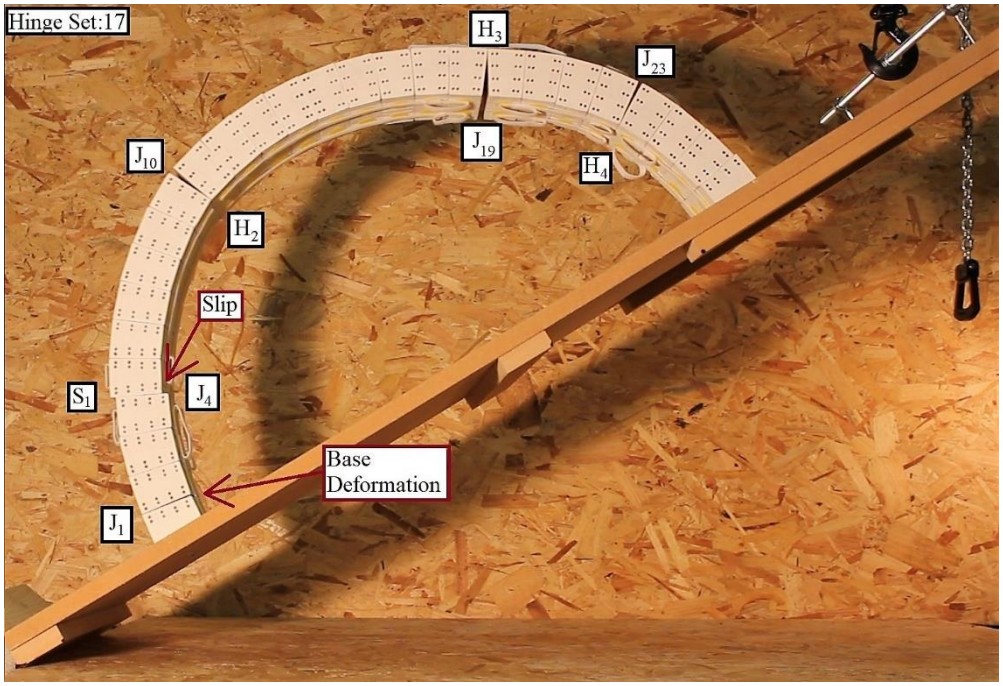

Fig. 24 Image of the Type II mechanism and observable base deformation

6 Post-Processing and Validation

From the experimental results it is clear that a capacity adjustment is required to more accurately match the models to the experimentation. Additionally, the Type II mechanism must be assessed.

6.1 Capacity Adjustment Equation

For all three conditions seen in Fig. 22, the dominance of capacity is clearly controlled by the position of H_1. This dominance coupled with the observed base deformations requires a further investigation of the relationship between the two models and the experimental results. Therefore, the ratio between experimental and modelled results for each hinge set were taken. These ratios were then averaged for fixed H_1 positions. Figure 25 shows the plot of these averaged ratios against the H_1 position for both the LA and DEM models. From Fig. 25 it is apparent that there is a strong linearity between capacity ratios and hinge H_1's location for both. This linearity establishes a simple method to adjust capacity. The capacity adjustment equation for the LA model is

$$C_{LA} = -0.0603 \cdot H_1 + 0.871 \tag{14}$$

and the capacity adjustment equation for the DEM analysis is

$$C_{DEM} = -0.0989 \cdot H_1 + 1.142 \tag{15}$$

Note that H_1 equal to J_1 is not included in Fig. 25 because no reinforced base joints exist for this condition.

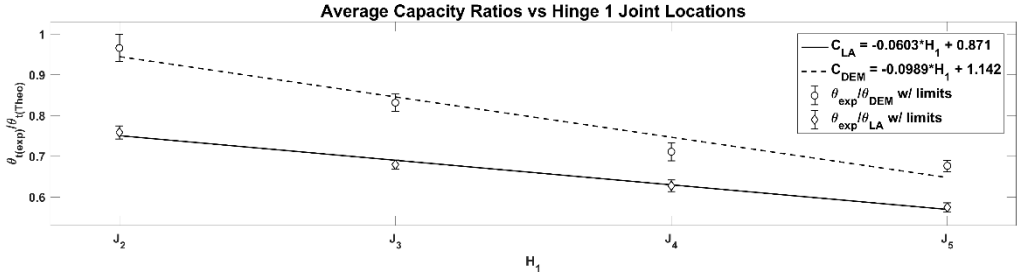

Fig. 25 Ratio of the averaged experimental and theoretical collapse angles versus H_1 joint location with linear fits

Considering the strong linearity in Fig. 25, the two observed cases of variations from the ideal (ie. Slip at H_1 and base deformation) and the fact that the slip condition was not present for all collapses, it is postulated that this strength reduction relationship is driven by non-infinite hinge stiffness of the Velcro® reinforcement at the base. The linear fits thus produce capacity compensation equations that are justified and can be applied to the models. Figure 26 shows the updated results with the capacity compensation equations applied.

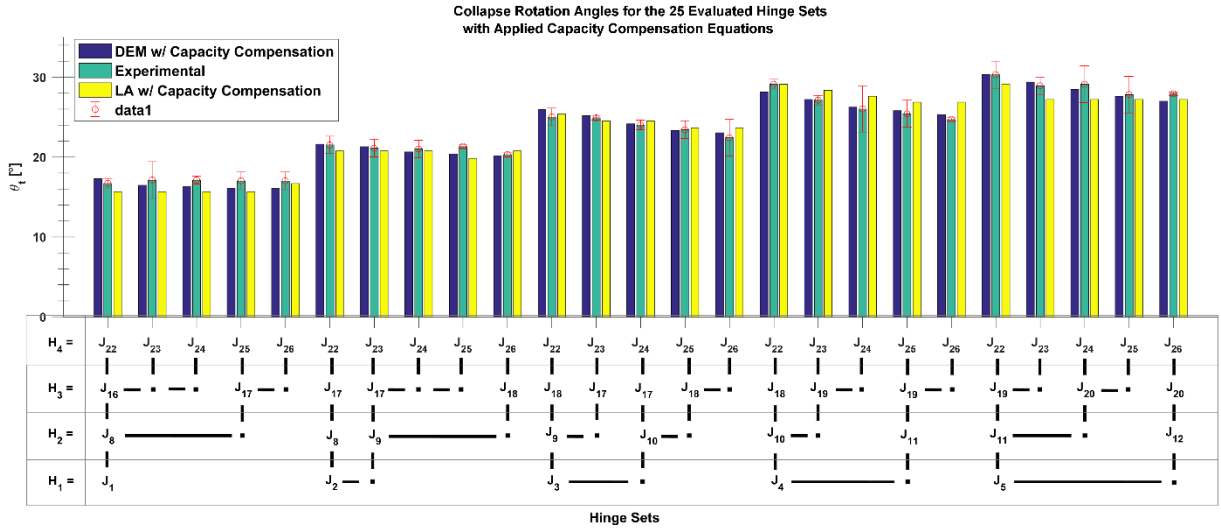

Fig. 26 Experimental, LA and DEM obtained collapse rotation angles versus hinge sets with the capacity compensation equations C_{LA} and C_{DEM} applied to the models respectively.

From Figs. 25 and 26, it becomes clear that the observed base deformations dominate the capacity of the system, but by evaluating a family of mechanisms that exist for the arch, the required compensation can be achieved through the evaluation of mechanical sets with the same H_1 locations. Additionally, the identification of the error and the validation of the results indicate that an improved hinge reinforcement system, such as FRPs or TRMs, has the potential to increase the capacity of the arch up to a factor of 3.2 times its minimum with the reinforcement applied as shown in Fig. 23.

6.2 Type II Mechanism and the Friction Angle

Although the base deformations dominated capacity and the discrepancy between the models and experimental results, the observation of the Type II mechanism must be addressed. The inclusion of slip at H_1 means that the static friction was exceeded. Therefore, a friction value must be obtained. To obtain a friction value, the standard equilibrium equation set was adjusted such that a moment at H_1 replaced the collapse multiplier in the reaction vector **r** and the collapse multiplier was incorporated into the constants vector **q**. Applying this modified equation set to the hinge sets and collapse values associated with H_1 at J_4, and utilizing Eqns. 5 through 7 produce a resulting friction angle associated with the collapse condition. Averaging these calculated friction angles produced a value of 17.6° ± 3°. The accepted friction angles for wood-wood contact are between 11° and 27° and thus the calculated value falls within the accepted range.

6.3 Adaptation of LA Model

The capacity compensation equation and Type II mechanism check was incorporated into the custom KCLC designed for the experiment. Evaluation of the hinge sets revealed that with the inclusion of the Type II mechanism and the calculated friction angle of 17.6° produced only admissible cases for H_1 greater than J_3. Figure 27 shows the KCLC evaluation for hinge set 20 (see Table 2). From Fig. 27, it can be seen that the difference between the Type II mechanism and the Type I with the applied capacity compensation equation is 0.3°. In fact, for all five hinge sets with a H_1 equal to J_4 the maximum difference between the two collapse angles is 1°. Consequently, the equivalent capacities of the Type II and capacity compensation for H_1 equal to J_4 coupled with the calculated friction angle within the range accepted for wood-wood interaction provides a sound validation of the LA approach and the inclusion of additional mechanism types.

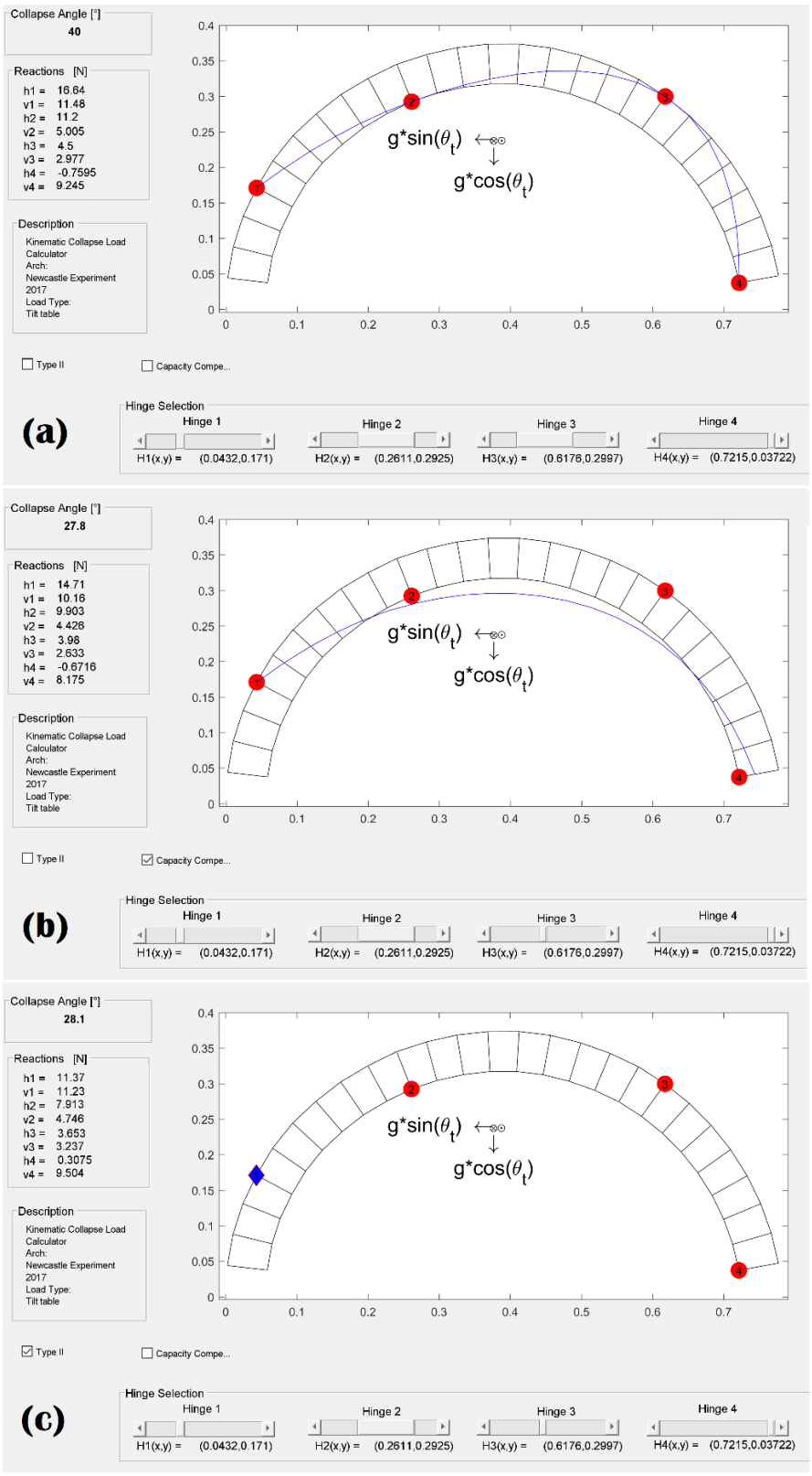

Fig. 27 Adapted KCLC for the experimental arch with the (a) standard evaluation, the (b) application of the capacity compensation equation and (a) the application of the Type II mechanism evaluation

7 Limiting Condition

From Section 3 of this work it was demonstrated that non-ideal conditions can be incorporated into the LA model used to construct the KCLC and that additional mechanism types can exist. The same principles used to establish the LA model for the observed Type II mechanism were then employed to establish Types III through VII. Now the consideration of the limiting condition analysis for a given arch-hinge set must be incorporated into the analysis platform.

The limiting conditions evaluation considers all the selected mechanism types and identifies the limiting condition. Deselecting the minimum condition then switches the KCLC to the next minimum and so on. In this way, all of the admissible mechanisms can be considered for a given arch-hinge set in ascending order. This process is highlighted in Fig. 28. Note that in Fig. 28, which reflects the generalized conditions of the experimental arch, the Type VII mechanism is the limiting condition, but it was not observed in the experimentation. The reason for this discrepancy is that the intermediate hinges, H_2 and H_3, develop before collapse and thus define Type VII as non-admissible before its capacity is reached (see Fig. 29). This is most likely due to a combination of geometric irregularities and the observed base deformation, but it does indicate the potential for the application of reinforcement to produce a weaker arch.

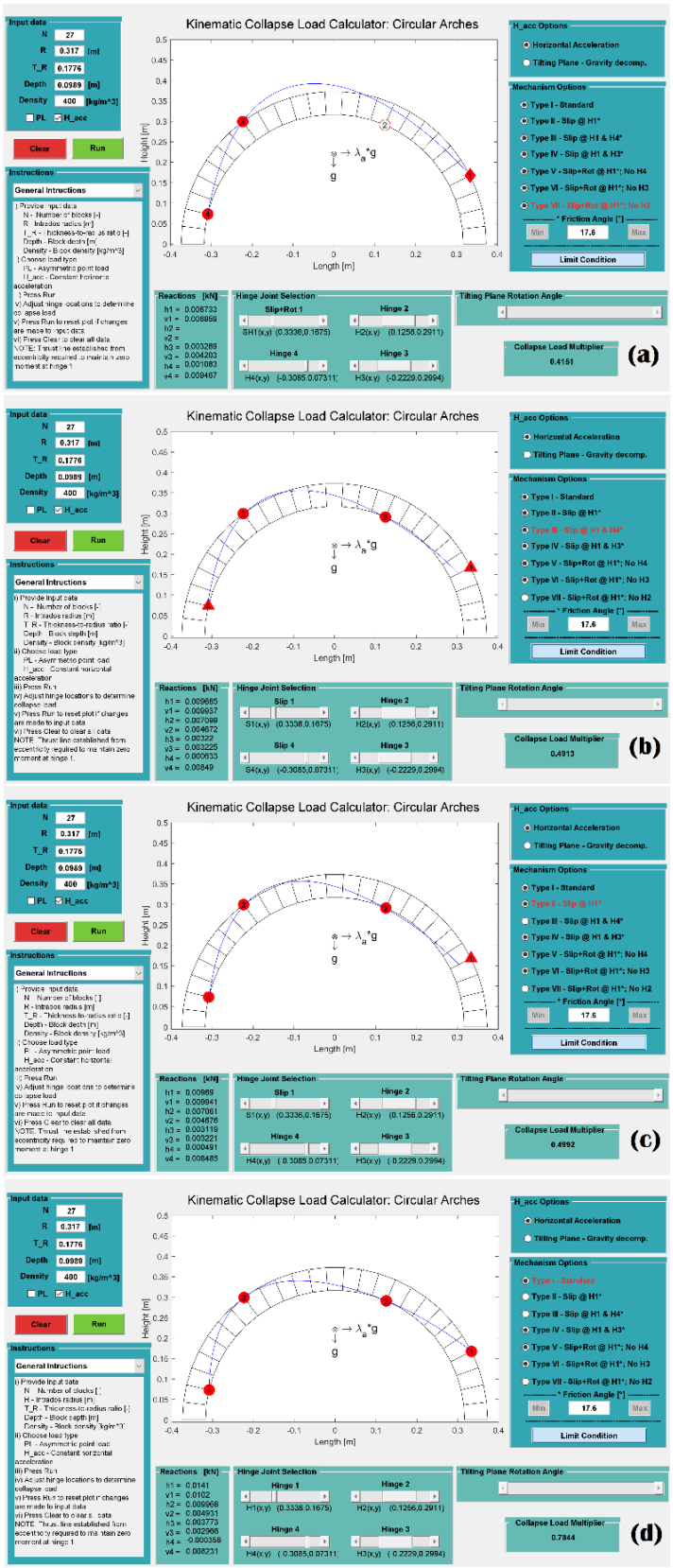

Fig. 28 Limit condition evaluation of generalized arch similar to the experimental conditions with (a) Type VII controlling, followed by (b) Type IV, (c) Type III and lastly (d) Type I.

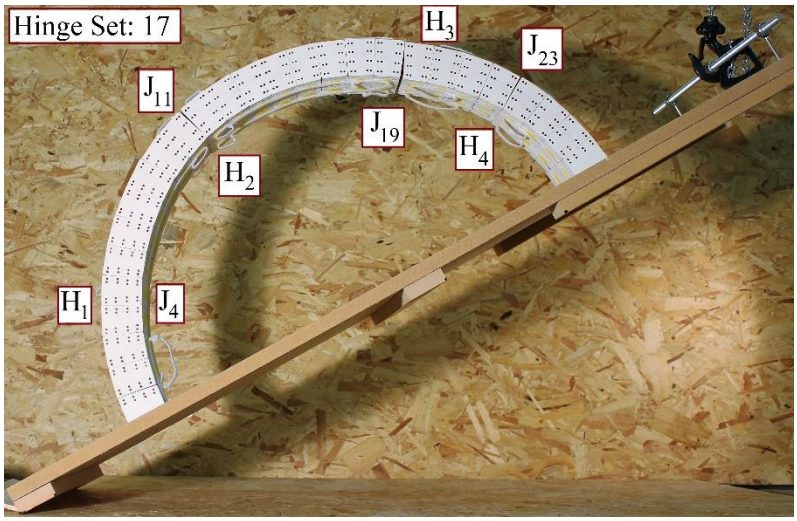

Fig. 29 Three-hinged stable state rendering Type III and Type VII mechanisms as non-admissible

Also seen in Fig. 28 is that the Type II and Type III mechanism have generally the same capacities for the specific condition, but only the Type II mechanism was observed experimentally. This again is most likely the consequence of the geometric irregularities and the observed base deformation which results in the pre-failure hinge formations. The inclusion of additional mechanism types thus presents the landscape of evaluations to consider, but it does not remove the need for sound engineering judgment when applied to physical systems.

7.1 Generic Arches

Utilizing the data extraction technique developed by Stockdale and Milani (2018b), the KCLC can also be extended beyond the circular. Figures 30 and 31 show the limiting condition sequence applied to a tapered arch after the friction angle was determined for the Type II mechanism and given hinge set.

Figure 32 shows another example where the limiting condition sequence is applied to a lancet arch. This limiting sequence is notable in the small variances in all the admissible mechanism and that Types I and VII have equivalent capacities. Between the various arches considered, both the versatility of the approach and the importance of extending the evaluation beyond the standard four hinge mechanism is observed.

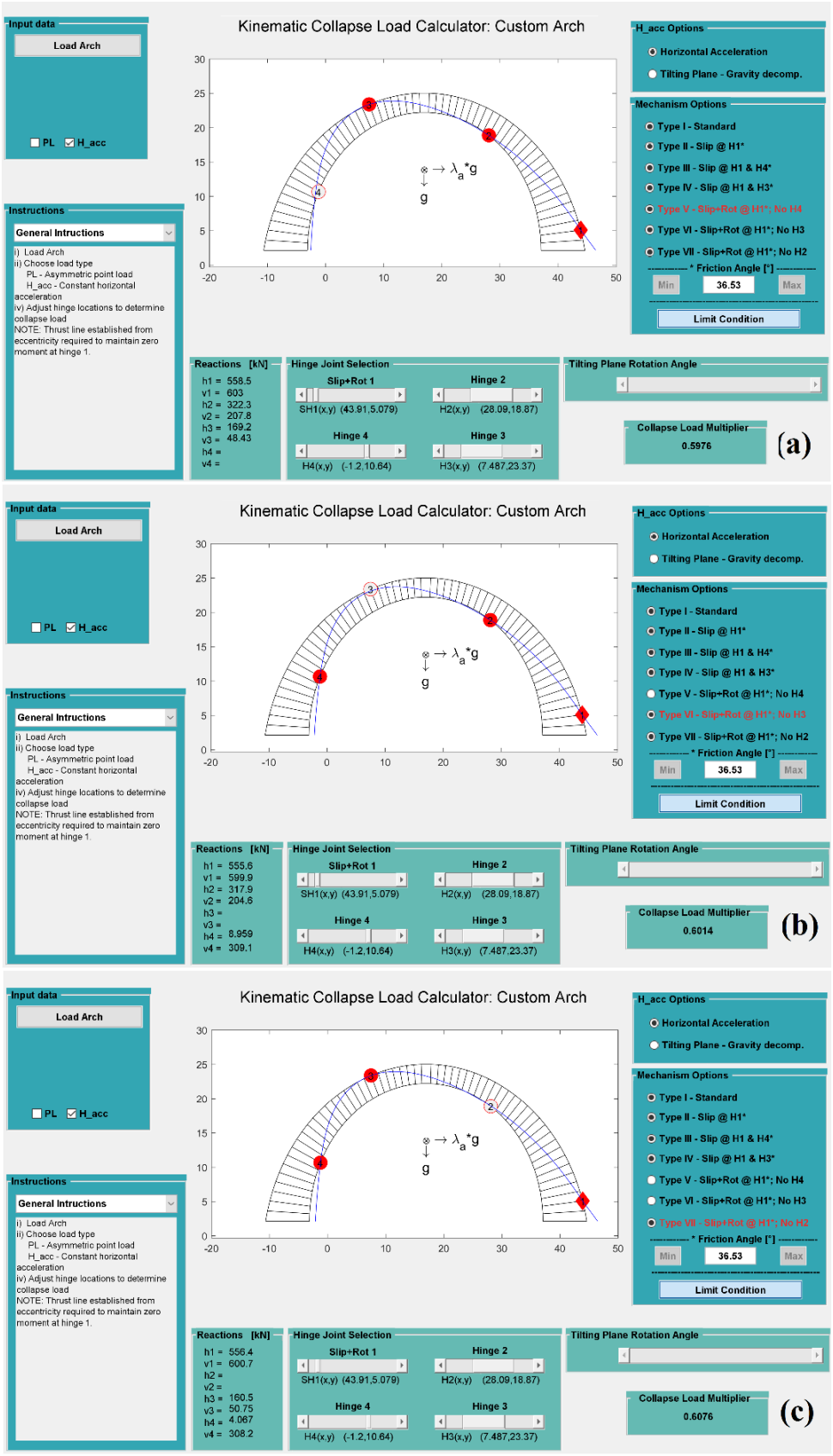

Fig. 30 Limiting condition sequence steps (a) 1, (b) 2 and (c) 3 for a double curvature arch

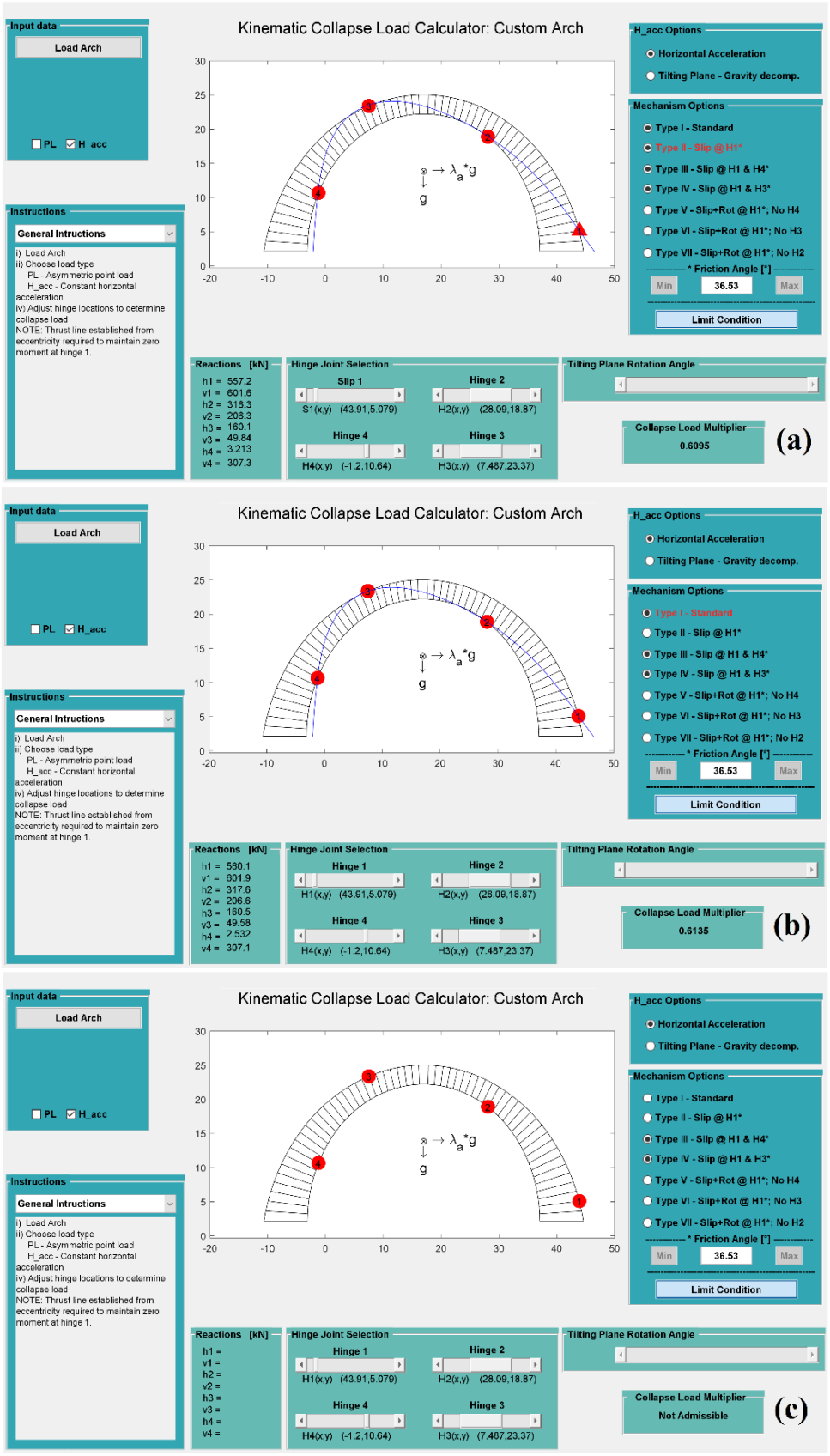

Fig. 31 Limiting condition sequence steps (a) 4, (b) 5 and (c) the non-admissible end for a double curvature arch

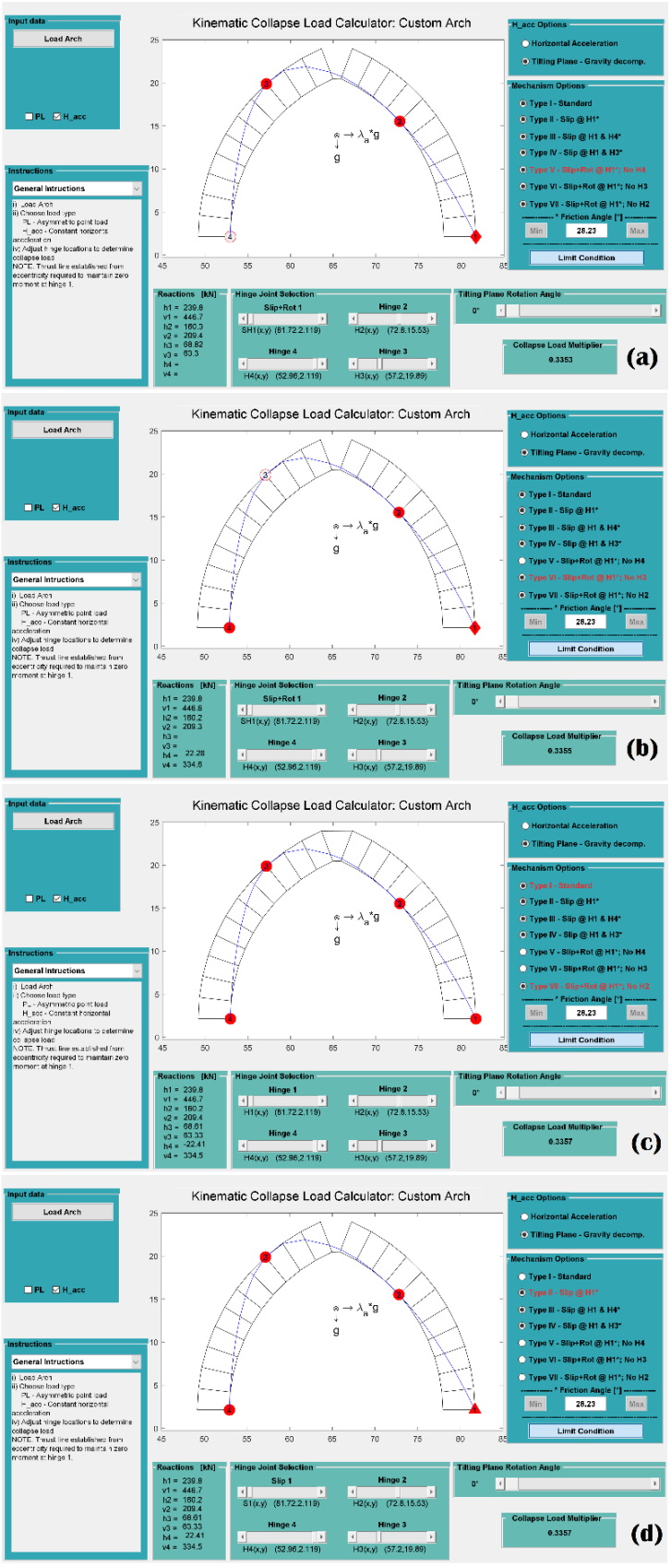

Fig. 32 Limiting condition sequence for a lancet arch.

8 Capacity Compensation for Non-Stable Admissible Mechanisms

Figure 23 shows the identified unstable zones and minimum flexural hinge reinforcement required to obtain the maximum measured capacity of the tested hinge configurations. The minimum reinforcement reveals the transformation of the kinematic system from the minimum condition. To better understand the minimum application, further consideration must be given to the relationship between the arch and the thrust line.

Stability is defined through the existence of a trust line that lies entirely within the material boundaries of the arch, whereas kinematic admissibility considers establishing the condition of motion. The condition of motion itself only places boundary conditions on the thrust line at the mechanical joints. This allows the thrust line in its traditional consideration to exist outside the material boundaries of the arch. The thrust line however is a physical phenomenon as observed through the hanging chain and its existence outside the material of the arch is prohibited. Therefore, the line of thrust for a kinematically admissible non-stable configuration must be adjusted to lie entirely within the material boundary.

To achieve this thrust line adjustment, Eqn. 5 is utilized at each block joint where the thrust line lies outside the material boundary. This thrust line adjustment thus introduces a joint based moment capacity requirement necessary to obtain the non-stable admissible mechanism. This joint based moment requirement can then be achieved through the application of a flexural hinge reinforcement technique. If a tensile reinforcement is applied to the external surface of the arch, then the required tensile capacity, *T*, of the reinforcement can be determined by;

$$T_i = M_i \cdot t_i \tag{16}$$

for the i^{th} joint with thickness *t*. Thus, the minimum reinforcement configuration and capacity can be established.

This capacity compensation strategy was implemented into the KCLC through the thrust line adjustment and identifying markers for joints where the traditional thrust line lies outside a boundary as can be seen in Fig. 33 for the tensile compensation condition. A thrust line tracker was also created to obtain the forces at each joint, including any required capacity compensation. In this manner the optimization of reinforcement can be determined.

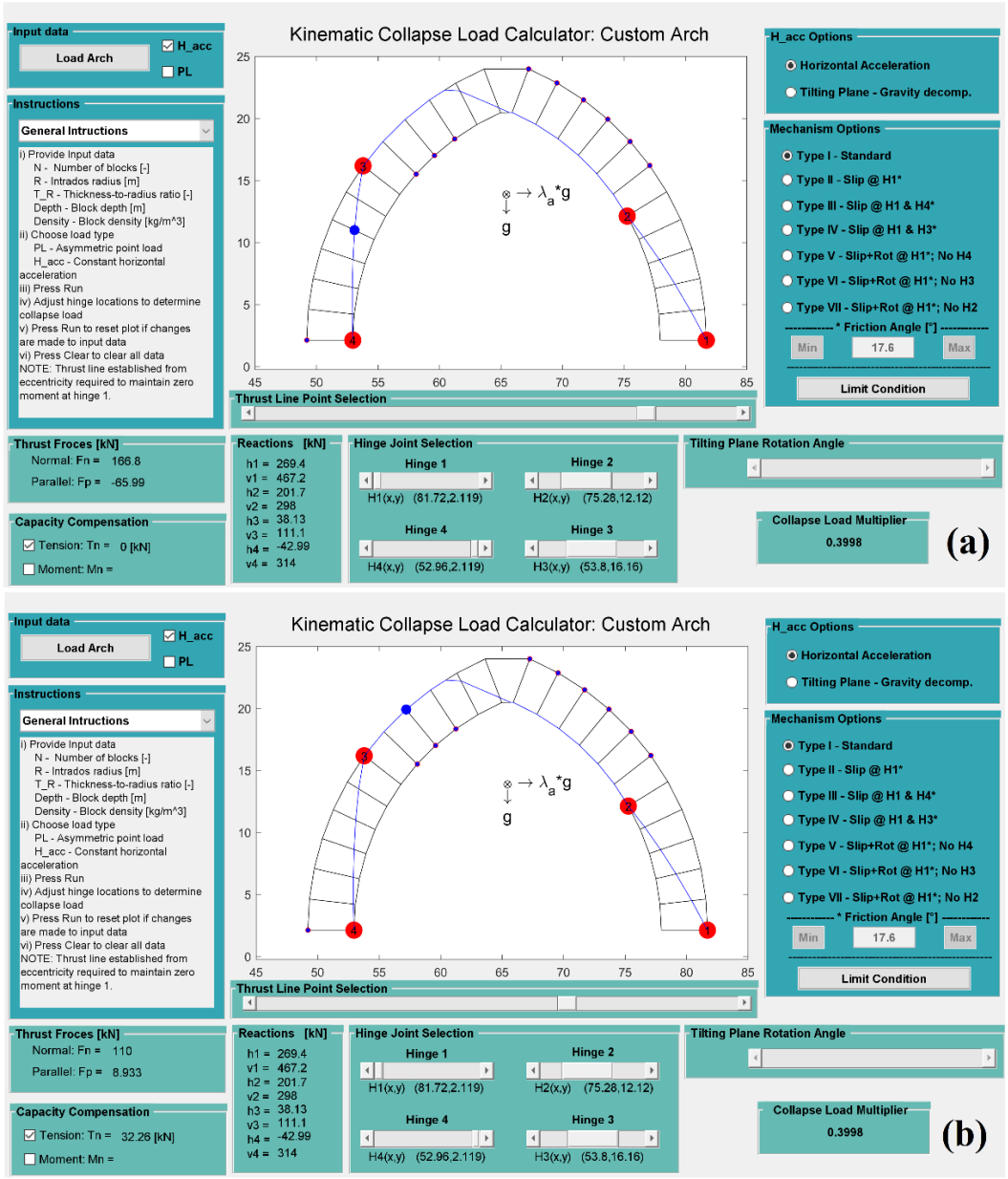

Fig. 33 Capacity compensation for a lancet arch and defined hinge combination with a (a) stable and (b) non-stable joint under tensile compensation

Finally, the concept of the limiting condition combined with the capacity compensation through thrust line adjustments further reveals the potential to reduce an arches capacity from reinforcing the arch. Figure 34 shows the comparison of the Type VII and Type I mechanisms for the tapered arch. From this figure the importance of the reinforcement strategy is clear.

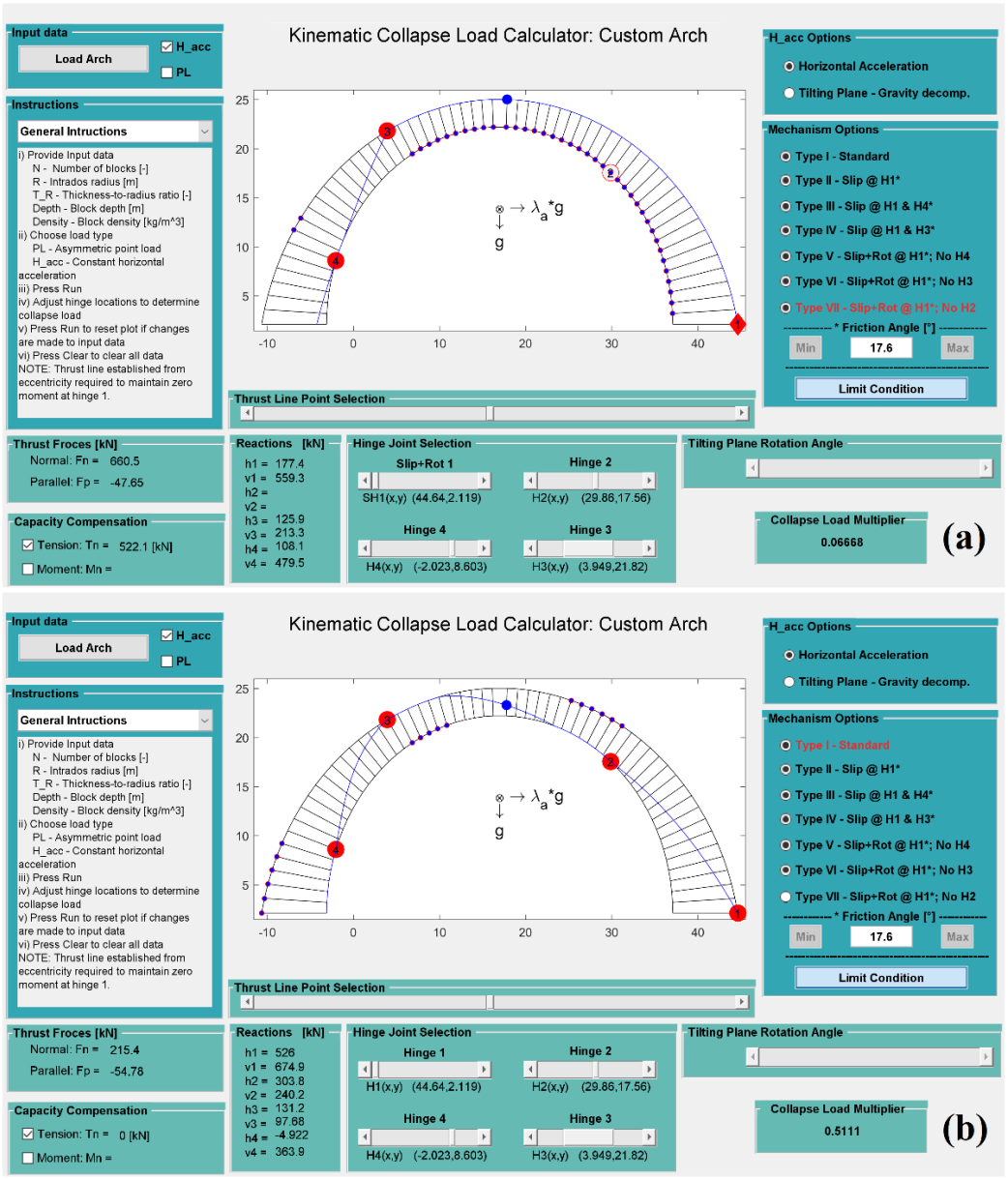

Fig. 34 Comparison of the capacity compensation required for the (a) Type VII and (b) Type I mechanisms for a tapered arch with the given hinge configuration

9 Conclusions

Seismic assessment and the retrofitting of masonry arches is critical and effective and efficient static assessment strategies must be employed. Constant horizontal accelerations provide a suitable method to establish static seismic assessments and the tilting plane test is a cheap and effective strategy to experimentally impose them. Additionally, the common flexural hinge reinforcement strategies focus on the full transformation from stability to strength for the masonry arch. This results in an incomplete understanding of the stability to strength transformation process. The diversity of materials and ages of masonry also complicates the predictability of a system when fully transformed.

The analysis of unreinforced masonry arches has focused on determining the limiting mechanism, but that is changing. The ability to control the mechanism now exists and the significant gap between mechanization and material strength provides the potential to define and design failure. This expands the focus from the minimum problem to the assessment of admissible mechanisms. The KCLC and its fundamental structure have been

developed directly from the structure of statics, but instead of examining the existence of equilibrium in a stable state, it examines equilibrium of a mechanical state at rest. The simplicity and efficiency of the analysis method is clear, but it must adapt and grow beyond the ideal conditions. The ability to execute a tilting plane analysis must exist to link experimentation and analysis, and the inclusion of mechanisms that arise with the removal of the no-slip condition must be evaluated.

The mechanism and tilting plane adaptations to the KCLC and the LA model were first presented. These adaptations included gravity decomposition and six additional mechanism types. The family of mechanism types was derived from the experimental observation of a well-defined slip-hinge combination failure. After presenting the adaptations, the experimental campaign driving them was presented in detail and included a customized KCLC model and a DEM analysis as well. The initial results showed a significant discrepancy in the capacities of the models and experiment, but the base deformation error was identified, and the models were adjusted through capacity compensation equations. After this adjustment, the observed Type II mechanism was addressed and a friction value consistent with a wood-wood interface was obtained. This Type II mechanism with the calculated friction angle and the capacity compensation equation were then applied to the custom KCLC. The analysis then revealed a tool that matched the capacity and behaviour of the experimental collapse condition, and that the capacity of the Type II mechanism and the reduced capacity from the base deformations intersect at the onset of the observed Type II mechanism dominance. The limiting condition evaluation of the full set of mechanism types was then discussed and revealed how the imperfections of an arch play a role in defining the limiting mechanism. Lastly, a capacity compensation strategy was employed that arose from non-stable kinematically admissible mechanisms and the traditional consideration of the thrust line. This capacity compensation then produces the ability to optimize the application of flexural hinge reinforcement and further highlights the need for sound engineering judgment.

Whether designing a new arch or assessing an existing one, the developed KCLC presented in this work provides a platform for practitioners to easily and efficiently asses an arches seismic capacity and develop reinforcement strategies based upon mechanizations. The behaviour of masonry arches does not fall into the simple nature of linear elasticity and KCLC provides the platform to circumvent this hurdle. The software provides the structural analysis information from which engineering judgement can be applied.

The development of the KCLC and supporting LA model must continue to grow and expand. The seven mechanisms are only a fraction of the full set that exists with the inclusion of slip. While they may be rare, they cannot not be ignored. The loading conditions need to expand, potential infill has to be addressed and more experimental testing is necessary. Additionally, while the base deformations were identified and corrected for validation, the consequence of a finite hinge reinforcement stiffness needs to be accounted for and directly incorporated into the model. Then the expansion to three-dimensions can begin.

Acknowledgement
This research was partially supported by the Global Challenge Research Fund provided by British Academy (CI170241). We also thank our colleagues from Newcastle University who provided insight and expertise in the area of experimental testing.

Appendix A – Equilibrium Equations

A.1 Notation List

$[BC_j]$ – Balance matrix for mechanism Type j

f_{gi} – Gravitational force of element i

h_a – Horizontal reaction force for hinge point a

M_a – Reaction moment for slip joint a

$\{q_j\}$ – Constants vector for mechanism Type j

$\{r_j\}$ – Reaction vector for mechanism Type j

v_a – Vertical reaction force at hinge point a

α_a – Angle relationship between the reaction vector, block boundary line and friction angle for slip joint a (see Sections 2.3 and 2.4)

$\Delta x_{a,b}$ – Horizontal difference between hinge points a and b

$\Delta x_{CMi,b}$ – Horizontal distance between element i's center of mass and hinge point a

$\Delta y_{a,b}$ – Vertical difference between hinge points b and a

$\Delta y_{CMi,b}$ – Vertical difference between element i's center of mass and hinge point b

λ_a – Collapse multiplier for constant horizontal acceleration

θ_t – Tilting plane rotation angle

A.2 Type I Mechanism – Horizontal Acceleration

$$[BC_I] = \begin{bmatrix} -1 & 0 & 1 & 0 & 0 & 0 & 0 & 0 & f_{g1} \\ 0 & 1 & 0 & -1 & 0 & 0 & 0 & 0 & 0 \\ 0 & 0 & -\Delta y_{2,1} & \Delta x_{1,2} & 0 & 0 & 0 & 0 & -f_{g1}\Delta y_{CM1,1} \\ 0 & 0 & -1 & 0 & 1 & 0 & 0 & 0 & f_{g2} \\ 0 & 0 & 0 & 1 & 0 & 1 & 0 & 0 & 0 \\ 0 & 0 & 0 & 0 & \Delta y_{3,2} & \Delta x_{2,3} & 0 & 0 & f_{g2}\Delta y_{2,CM2} \\ 0 & 0 & 0 & 0 & -1 & 0 & 1 & 0 & f_{g3} \\ 0 & 0 & 0 & 0 & 0 & -1 & 0 & 1 & 0 \\ 0 & 0 & 0 & 0 & 0 & 0 & \Delta y_{3,4} & -\Delta x_{3,4} & f_{g3}\Delta y_{3,CM3} \end{bmatrix}$$

$$\{r_I\} = \begin{bmatrix} h_1 \\ v_1 \\ h_2 \\ v_2 \\ h_3 \\ v_3 \\ h_4 \\ v_4 \\ \lambda_a \end{bmatrix} \qquad \{q_I\} = \begin{bmatrix} 0 \\ f_{g1} \\ -f_{g1}\Delta x_{1,CM1} \\ 0 \\ f_{g2} \\ f_{g2}\Delta x_{2,CM2} \\ 0 \\ f_{g3} \\ -f_{g3}\Delta x_{3,CM3} \end{bmatrix}$$

A.3 Type I Mechanism – Horizontal Acceleration & Gravity Decomposition

$$[BC_{It}] = \begin{bmatrix} -1 & 0 & 1 & 0 & 0 & 0 & 0 & 0 & f_{g1} \\ 0 & 1 & 0 & -1 & 0 & 0 & 0 & 0 & 0 \\ 0 & 0 & -\Delta y_{2,1} & \Delta x_{1,2} & 0 & 0 & 0 & 0 & -f_{g1}\Delta y_{CM1,1} \\ 0 & 0 & -1 & 0 & 1 & 0 & 0 & 0 & f_{g2} \\ 0 & 0 & 0 & 1 & 0 & 1 & 0 & 0 & 0 \\ 0 & 0 & 0 & 0 & \Delta y_{3,2} & \Delta x_{2,3} & 0 & 0 & f_{g2}\Delta y_{2,CM2} \\ 0 & 0 & 0 & 0 & -1 & 0 & 1 & 0 & f_{g3} \\ 0 & 0 & 0 & 0 & 0 & -1 & 0 & 1 & 0 \\ 0 & 0 & 0 & 0 & 0 & 0 & \Delta y_{3,4} & -\Delta x_{3,4} & f_{g3}\Delta y_{3,CM3} \end{bmatrix}$$

$$\{r_{It}\} = \begin{bmatrix} h_1 \\ v_1 \\ h_2 \\ v_2 \\ h_3 \\ v_3 \\ h_4 \\ v_4 \\ \lambda_a \end{bmatrix} \qquad \{q_{It}\} = \begin{bmatrix} -f_{g1}\sin(\theta_t) \\ f_{g1}\cos(\theta_t) \\ -f_{g1}\cos(\theta_t)\,\Delta x_{1,CM1} + f_{g1}\sin(\theta_t)\,\Delta y_{CM1,1} \\ -f_{g2}\sin(\theta_t) \\ f_{g2}\cos(\theta_t) \\ f_{g2}\cos(\theta_t)\,\Delta x_{2,CM2} + f_{g2}\sin(\theta_t)\,\Delta y_{2,CM2} \\ -f_{g3}\sin(\theta_t) \\ f_{g3}\cos(\theta_t) \\ -f_{g3}\cos(\theta_t)\,\Delta x_{3,CM3} + f_{g3}\sin(\theta_t)\Delta y_{3,CM3} \end{bmatrix}$$

A.4 Type II Mechanism – Horizontal Acceleration

$$[BC_{II}] = \begin{bmatrix} -1 & 0 & 1 & 0 & 0 & 0 & 0 & 0 & f_{g1} & 0 \\ 0 & 1 & 0 & -1 & 0 & 0 & 0 & 0 & 0 & 0 \\ 0 & 0 & -\Delta y_{2,1} & \Delta x_{1,2} & 0 & 0 & 0 & 0 & -f_{g1}\Delta y_{CM1,1} & -1 \\ 0 & 0 & -1 & 0 & 1 & 0 & 0 & 0 & f_{g2} & 0 \\ 0 & 0 & 0 & 1 & 0 & 1 & 0 & 0 & 0 & 0 \\ 0 & 0 & 0 & 0 & \Delta y_{3,2} & \Delta x_{2,3} & 0 & 0 & f_{g2}\Delta y_{2,CM2} & 0 \\ 0 & 0 & 0 & 0 & -1 & 0 & 1 & 0 & f_{g3} & 0 \\ 0 & 0 & 0 & 0 & 0 & -1 & 0 & 1 & 0 & 0 \\ 0 & 0 & 0 & 0 & 0 & 0 & \Delta y_{3,4} & -\Delta x_{3,4} & f_{g3}\Delta y_{3,CM3} & 0 \\ -\tan(\alpha_1) & 1 & 0 & 0 & 0 & 0 & 0 & 0 & 0 & 0 \end{bmatrix}$$

$$\{r_{II}\} = \begin{bmatrix} h_1 \\ v_1 \\ h_2 \\ v_2 \\ h_3 \\ v_3 \\ h_4 \\ v_4 \\ \lambda_a \\ M_1 \end{bmatrix} \qquad \{q_{II}\} = \begin{bmatrix} 0 \\ f_{g1} \\ -f_{g1}\Delta x_{1,CM1} \\ 0 \\ f_{g2} \\ f_{g2}\Delta x_{2,CM2} \\ 0 \\ f_{g3} \\ -f_{g3}\Delta x_{3,CM3} \\ 0 \end{bmatrix}$$

A.5 Type III Mechanism – Horizontal Acceleration

$$[BC_{III}] = \begin{bmatrix} -1 & 0 & 1 & 0 & 0 & 0 & 0 & 0 & f_{g1} & 0 & 0 \\ 0 & 1 & 0 & -1 & 0 & 0 & 0 & 0 & 0 & 0 & 0 \\ 0 & 0 & -\Delta y_{2,1} & \Delta x_{1,2} & 0 & 0 & 0 & 0 & -f_{g1}\Delta y_{CM1,1} & -1 & 0 \\ 0 & 0 & -1 & 0 & 1 & 0 & 0 & 0 & f_{g2} & 0 & 0 \\ 0 & 0 & 0 & 1 & 0 & 1 & 0 & 0 & 0 & 0 & 0 \\ 0 & 0 & 0 & 0 & \Delta y_{3,2} & \Delta x_{2,3} & 0 & 0 & f_{g2}\Delta y_{2,CM2} & 0 & 0 \\ 0 & 0 & 0 & 0 & -1 & 0 & 1 & 0 & f_{g3} & 0 & 0 \\ 0 & 0 & 0 & 0 & 0 & -1 & 0 & 1 & 0 & 0 & 0 \\ 0 & 0 & 0 & 0 & 0 & 0 & \Delta y_{3,4} & -\Delta x_{3,4} & f_{g3}\Delta y_{3,CM3} & 0 & -1 \\ \tan(\alpha_1) & -1 & 0 & 0 & 0 & 0 & 0 & 0 & 0 & 0 & 0 \\ 0 & 0 & 0 & 0 & 0 & 0 & \tan(\alpha_4) & -1 & 0 & 0 & 0 \end{bmatrix}$$

$$\{r_{III}\} = \begin{bmatrix} h_1 \\ v_1 \\ h_2 \\ v_2 \\ h_3 \\ v_3 \\ h_4 \\ v_4 \\ \lambda_a \\ M_1 \\ M_4 \end{bmatrix} \qquad \{q_{III}\} = \begin{bmatrix} 0 \\ f_{g1} \\ -f_{g1}\Delta x_{1,CM1} \\ 0 \\ f_{g2} \\ f_{g2}\Delta x_{2,CM2} \\ 0 \\ f_{g3} \\ -f_{g3}\Delta x_{3,CM3} \\ 0 \\ 0 \end{bmatrix}$$

A.6 Type IV Mechanism – Horizontal Acceleration

$$[BC_{IV}] = \begin{bmatrix} -1 & 0 & 1 & 0 & 0 & 0 & 0 & 0 & f_{g1} & 0 & 0 \\ 0 & 1 & 0 & -1 & 0 & 0 & 0 & 0 & 0 & 0 & 0 \\ 0 & 0 & -\Delta y_{2,1} & \Delta x_{1,2} & 0 & 0 & 0 & 0 & -f_{g1}\Delta y_{CM1,1} & -1 & 0 \\ 0 & 0 & -1 & 0 & 1 & 0 & 0 & 0 & f_{g2} & 0 & 0 \\ 0 & 0 & 0 & 1 & 0 & 1 & 0 & 0 & 0 & 0 & 0 \\ 0 & 0 & 0 & 0 & \Delta y_{3,2} & \Delta x_{2,3} & 0 & 0 & f_{g2}\Delta y_{2,CM2} & 0 & 1 \\ 0 & 0 & 0 & 0 & -1 & 0 & 1 & 0 & f_{g3} & 0 & 0 \\ 0 & 0 & 0 & 0 & 0 & -1 & 0 & 1 & 0 & 0 & 0 \\ 0 & 0 & 0 & 0 & 0 & 0 & \Delta y_{3,4} & -\Delta x_{3,4} & f_{g3}\Delta y_{3,CM3} & 0 & -1 \\ \tan(\alpha_1) & -1 & 0 & 0 & 0 & 0 & 0 & 0 & 0 & 0 & 0 \\ 0 & 0 & 0 & 0 & \tan(\alpha_3) & -1 & 0 & 0 & 0 & 0 & 0 \end{bmatrix}$$

$$\{r_{IV}\} = \begin{bmatrix} h_1 \\ v_1 \\ h_2 \\ v_2 \\ h_3 \\ v_3 \\ h_4 \\ v_4 \\ \lambda_a \\ M_1 \\ M_3 \end{bmatrix} \qquad \{q_{IV}\} = \begin{bmatrix} 0 \\ f_{g1} \\ -f_{g1}\Delta x_{1,CM1} \\ 0 \\ f_{g2} \\ f_{g2}\Delta x_{2,CM2} \\ 0 \\ f_{g3} \\ -f_{g3}\Delta x_{3,CM3} \\ 0 \\ 0 \end{bmatrix}$$

A.7 Type V Mechanism – Horizontal Acceleration

$$[BC_V] = \begin{bmatrix} -1 & 0 & 1 & 0 & 0 & 0 & f_{g1} \\ 0 & 1 & 0 & -1 & 0 & 0 & 0 \\ 0 & 0 & -\Delta y_{2,1} & \Delta x_{1,2} & 0 & 0 & -f_{g1}\Delta y_{CM1,1} \\ 0 & 0 & -1 & 0 & 1 & 0 & f_{g2} \\ 0 & 0 & 0 & 1 & 0 & 1 & 0 \\ 0 & 0 & 0 & 0 & \Delta y_{3,2} & \Delta x_{2,3} & f_{g2}\Delta y_{2,CM2} \\ \tan(\alpha_1) & 1 & 0 & 0 & 0 & 0 & 0 \end{bmatrix}$$

$$\{r_V\} = \begin{bmatrix} h_1 \\ v_1 \\ h_2 \\ v_2 \\ h_3 \\ v_3 \\ \lambda_a \end{bmatrix} \qquad \{q_V\} = \begin{bmatrix} 0 \\ f_{g1} \\ -f_{g1}\Delta x_{1,CM1} \\ 0 \\ f_{g2} \\ f_{g2}\Delta x_{2,CM2} \\ 0 \end{bmatrix}$$

A.8 Type VI Mechanism – Horizontal Acceleration

$$[BC_{VI}] = \begin{bmatrix} -1 & 0 & 1 & 0 & 0 & 0 & f_{g1} \\ 0 & 1 & 0 & -1 & 0 & 0 & 0 \\ 0 & 0 & -\Delta y_{2,1} & \Delta x_{1,2} & 0 & 0 & -f_{g1}\Delta y_{CM1,1} \\ 0 & 0 & -1 & 0 & 1 & 0 & f_{g2} + f_{g3} \\ 0 & 0 & 0 & 1 & 0 & 1 & 0 \\ 0 & 0 & 0 & 0 & \Delta y_{2,4} & -\Delta x_{2,4} & f_{g2}\Delta y_{2,CM2} + f_{g3}\Delta y_{2,CM3} \\ \tan(\alpha_1) & 1 & 0 & 0 & 0 & 0 & 0 \end{bmatrix}$$

$$\{r_{VI}\} = \begin{bmatrix} h_1 \\ v_1 \\ h_2 \\ v_2 \\ h_4 \\ v_4 \\ \lambda_a \end{bmatrix} \qquad \{q_{VI}\} = \begin{bmatrix} 0 \\ f_{g1} \\ -f_{g1}\Delta x_{1,CM1} \\ 0 \\ f_{g2} + f_{g3} \\ -f_{g2}\Delta x_{2,CM2} - f_{g3}\Delta x_{2,CM3} \\ 0 \end{bmatrix}$$

A.9 Type VII Mechanism – Horizontal Acceleration

$$[BC_{VII}] = \begin{bmatrix} -1 & 0 & 1 & 0 & 0 & 0 & f_{g1} + f_{g2} \\ 0 & 1 & 0 & -1 & 0 & 0 & 0 \\ 0 & 0 & -\Delta y_{3,1} & -\Delta x_{1,3} & 0 & 0 & -f_{g1}\Delta y_{CM1,1} - f_{g2}\Delta y_{CM2,1} \\ 0 & 0 & -1 & 0 & 1 & 0 & f_{g3} \\ 0 & 0 & 0 & 1 & 0 & 1 & 0 \\ 0 & 0 & 0 & 0 & \Delta y_{3,4} & -\Delta x_{3,4} & f_{g3}\Delta y_{3,CM3} \\ \tan(\alpha_1) & 1 & 0 & 0 & 0 & 0 & 0 \end{bmatrix}$$

$$\{r_{VII}\} = \begin{bmatrix} h_1 \\ v_1 \\ h_3 \\ v_3 \\ h_4 \\ v_4 \\ \lambda_a \end{bmatrix} \qquad \{q_{VII}\} = \begin{bmatrix} 0 \\ f_{g1} + f_{g2} \\ -f_{g1}\Delta x_{1,CM1} - f_{g2}\Delta x_{1,CM2} \\ 0 \\ f_{g3} \\ -f_{g3}\Delta x_{3,CM3} \\ 0 \end{bmatrix}$$

Appendix B – Recorded Data

Platform Measurements		precision			* M - MACHANISM
L1 [mm]	L2 [mm]	+/-	0.5	mm	S - SLIP
611	788				R - ROTATION
COLLAPSE DATA					

Run	Hinge Set	l1 [mm]	l2 [mm]	Failure type *	notes:
1	1	172	222	M	
2	1	190	247.5	M	
3	1	187	245	MS	SMALL S AT H1
4	1	188	245.5	M	
11	1	187	245	M	
5	2	187	245	M	
6	2	194	248	M	
7	2	174	227	MS	SMALL S AT H1
8	2	195	254	M	
9	2	174.5	227	M	
10	2	189	246	MS	MODERATE S AT H1
12	3	190	247	MS	MODERATE S AT H1
13	3	191	248	MS	MODERATE S AT H1
14	3	184	239.5	M	
15	3	183	238	M	
16	4	178.5	232.5	M	
17	4	203	295	MS	SMALL S AT H1
18	4	174	227	MSM	MECH-SLIP-MECH
19	4	181	235.5	M	
20	5	187	244	MS	VERY SMALL S AT H1
21	5	177	230	M	
22	5	182	238.5	MSM	MECH-SLIP-MECH
23	6	230	298.5	M	
24	6	246	320	MR	SMALL OUT OF PLANE ROTATION
25	6	243	313.5	M	GOOD M
26	7	228	295	M	
27	7	243	313.5	M	
28	7	237	307.5	M	

Run	Hinge Set	l1 [mm]	l2 [mm]	Failure type *	notes:
29	8	233	302	M	ALLIGNMENT LITTLE OFF AT H1
30	8	243.5	312	M	
31	8	228	295	M	
32	9	238.5	309.5	M	GOOD M AND DOT ALLIGNMENT
33	9	237.5	309	M	
34	9	235	305.5	M	ALLIGNMENT LITTLE OFF AT H1 AND H3
35	10	222.5	289	M	ALLIGNMENT OFF AT H1
36	10	228	296	M	ALLIGNMENT OFF AT H1 AND H2
37	10	225.5	293	SM	S AT H1 M BEGINS AT HALF BLOCK THICKNESS
38	11	248	322	M	
39	11	271	351	MRS	SMALL S AND R AT H1 THEN M
40	11	233	303	MS	SMALL S AT H1 FROM FIXED SECTION
41	12	256	334	MS	SMALL SLIP/SHIFT AT H1
42	12	259	336	M	
43	12	275	355.5	M	SMALL STATIC TWIST AT H3 AT START
44	13	264	341.5	MS	VERY SMALL S AT H1
45	13	275	356	MS	VERY SMALL S AT H1
46	13	275	356	SM	SMALL S AT H1 THEN M
47	14	281	364	SM	SMALL S AT H1 THEN M
48	14	281	364	SM	SMALL S AT H1 THEN M
49	14	285.5	369	SM	SMALL S AT H1 THEN M
50	15	292	377.5	SM	SMALL S AT H1 THEN M
51	15	283	366.5	SM	SMALL S AT H1 THEN M
52	15	279	362	SM	SMALL S AT H1 THEN M
53	16	346	447	MS	VERY SMALL S AT H1
54	16	337	436.5	MS	VERY SMALL S AT H1
55	16	337	435	MS	VERY SMALL S AT H1
56	17	315.5	409	SM	SMALL S AT H1 THEN M

Run	Hinge Set	l1 [mm]	l2 [mm]	Failure type *	notes:
57	17	315	407.5	SM	SMALL S AT H1 THEN M
58	17	307	398	SM	S AT H1 M BEGINS AT 1/2 BLOCK THICKNESS
59	18	301	392	SM	SMALL S AT H1 THEN M
60	18	314	416	SM	S AT H1 M BEGINS AT 1/2 BLOCK THICKNESS
61	18	275	355	SM	S AT H1 M BEGINS AT 1/2 BLOCK THICKNESS
62	19	296	383.5	SM	S AT H1 M BEGINS AT 1/2 BLOCK THICKNESS
63	19	300	388.5	SM	S AT H1 M BEGINS AT 1/2 BLOCK THICKNESS
64	19	273	355	SM	S AT H1 M BEGINS AT 1/2 BLOCK THICKNESS
65	20	280	363.5	SM	S AT H1 M BEGINS AT 1/2 BLOCK THICKNESS
66	20	279	363	SM	S AT H1 M BEGINS AT 1/2 BLOCK THICKNESS
67	20	282	365.5	SM	S AT H1 M BEGINS AT 1/2 BLOCK THICKNESS
68	21	321.5	417	M	SOME ROTATIONS AT J=1 RESTRAINED
69	21	322	418	M	SOME ROTATIONS AT J=1 RESTRAINED
70	21	323	419	M	SOME ROTATIONS AT J=1 RESTRAINED
71	22	339.5	439	M	LESS ROT AT J=1
72	22	314	406	M	LESS ROT AT J=1
73	22	313	404	M	LESS ROT AT J=2
74	23	324.5	423	M	LESS ROT AT J=2
75	23	351	454	M	LESS ROT AT J=2
76	23	343.5	442	M	LESS ROT AT J=2
77	24	336.5	435.5	M	LESS ROT AT J=1
78	24	326.5	422.5	M	SOME ROTATIONS AT J=1 RESTRAINED
79	24	339	439	M	SOME ROTATIONS AT J=1 RESTRAINED
80	25	364	469	MSR	H4 SLIDE-ROTATE, H1 SLIDE-ROTATE SOME TWIST
81	25	343	445	MSR	H4 SLIDE-ROTATE, H1 SLIDE-ROTATE SOME TWIST
82	25	363	468.5	MSR	H4 SLIDE-ROTATE, H1 SLIDE-ROTATE SOME TWIST

Table B1 Recorded experimental data

References

Alexakis H, Makris N (2014) Limit equilibrium analysis and the minimum thickness of circular masonry arches to withstand lateral inertial loading. Arch Appl Mech, **8** (5): 757-772

Alexandros L, Kouris S, Triantafillou TC (2018) State-of-the-art on strengthening of masonry structures with textile reinforced mortar (TRM). Construction and Building Materials, **188**: 1221-1233, DOI: 10.1016/j.conbuildmat.2018.08.039

Anania L and D'Agata G (2017) Limit Analysis of vaulted structures strengthened by an innovative technology in applying CFRP. Construction and Building Materials **145**: 336-346, DOI: 10.1016/j.conbuildmat.2017.03.212

Angelillo M (ed) (2014) Mechanics of Masonry Structures. Springer: London.

Bertolesi E, Milani G, Carozzi FG, Poggi C (2018) Ancient masonry arches and vaults strengthened with TRM, SRG and FRP composites: Numerical analyses. Composite Structures, **187**: 385-402

Bhattacharya S, Nayak S and Dutta SC (2014) A critical review of retrofitting methods for unreinforced masonry structures. Int J of Disaster Risk Reduction, **7**: 51-67

Borri A, Castori G and Corradi M (2011) Intrados strengthening of brick masonry arches with composite maerials. Composites: Part B, **42**: 1164-1172

Bui TT, Limam A, Sarhosis V, Hjiaj M. (2017) Discrete element modelling of the in-plane and out-of-plane behaviour of dry-joint masonry wall constructions. Engineering Structures, 136, 277-294.

Calderini C and Lagomarsino S (2014) Seismic Response of Masonry Arches Reinforced by Tie-Rods: Static Tests on a Scale Model. J. Struct. Eng., 2015, 141(5): -1—1, DOI: 10.1061/(ASCE)ST.1943-541X.0001079.

Cancelliere I, Imbimbo M and Sacco E (2010) Experimental tests and numerical modelling of reinforced masonry arches. Eng Struct, **32**: 776-792

Carozzi FG, Poggi C, Bertolesi E, Milani G (2018) Ancient masonry arches and vaults strengthened with TRM, SRG and FRP composites: Experimental evaluation. Composite Structurs, **187**: 466-480

Ceroni F, Salzano P (2018) Design provisions for FRCM systems bonded to concrete and masonry elements. Composites Part B: Engineering, **143**: 230-242

Clemente P (1998) Introduction to dynamics of stone arches. Earthq Eng Struct Dynam, **27** (5): 513-522

Cundall P.A. 1971. A Computer Model for Simulating Progressive Large Scale Movements in Blocky Rock Systems, in Proceedings of the Symposium of the International Society for Rock Mechanics, Nancy, France, 1, pp. 11-18.

DeJong M (2009) Seismic Assessment Strategies for Masonry Structures, PhD Dissertation, Massachusetts Institute of Technology, Massachusetts.

De Luca A, Giordano A, Mele E (2004) A simplified procedure for assessing the seismic capacity of masonry arches. Eng Struct, **26** (13): 1915-1929

De Santis S, de Felice G (2014) Overview of railway masonry bridges with a safety factor estimate. International Journal of Architectural Heritage, **8**(3) 452-474.

De Santis S, Hadad HA, De Caso y Basalo F, de Felice G and Nanni A (2018) Acceptance Criteria for Tensile Characterization of Fabric-Reinforces Cementitious Matrix Systems for Concrete and Masonry Repair. J. Compos. Constr., **22**(6): 04018048, DOI: 10.1061/(ASCE)CC.1943-5614.0000886

De Santis S, Roscini F and de Felice G (2018) Full-scale tests on masonry vaults strengthened with Steel Reinforced Grout. Composites Part B, **141**: 20-36,

Dimitri R., Tornabene F (2015) A parametric investigation of the seismic capacity for masonry arches and portals of different shapes. Eng Fail Anal, **52**: 1-34

Fanning PJ, Sobczak L, Boothby TE and Salomoni V (2005) Load testing and model simulations for a stone arch bridge. Bridge Structures, **1**(4): 367-378

Forgács T, Sarhosis V, Bagi K. Minimum thickness of semi-circular skewed masonry arches. Engineering Structures 2017, 140(1), 317–336.

Formisano, A., Marzo, A. (2017). Simplified and refined methods for seismic vulnerability assessment and retrofitting of an Italian cultural heritage masonry building. Computers and Structures, 180, pp. 13-26. DOI: 10.1016/j.compstruc.2016.07.005

Gaetani A, Lourenço PB, Monti G and Moroni M (2016) Shaking table tests and numerical analysis on a scaled dry-joint arch undergoing windowed sign pulses. Bull Earthquake Eng, DOI: 10.1007/s10518-017-0156-0

Gattesco N, Boem I and Adretta V (2018) Experimental behavior of non-structural masonry vaults reinforced through fibre-reinforced mortar coating and sujected to cyclic horizontal loads. Eng Struct, **172**: 419-431

Giamundo V., Sarhosis V., Lignola G.P., Sheng Y., Manfredi G., 2014. Evaluation of different computational strategies for modelling low strength masonry, Engineering Structures, 73, pp. 160-169.

Gilbert M, Melbourne C (1994) Rigid-block analysis of masonry structures. Struct Eng. 72(21)

Group, I.C. (2015) 3DEC version 5.00 Distinct-Element Modeling of Jointed and Blocky Material in 3D. Minneapolis.

Heydariha JZ, Ghaednia H, Nayak S, Das S, Bhattacharya S and Dutta SC (2019) Experimental and Field Performance of PP Band-Rertrofitted Masonry: Evaluation of Seismic Behaviour. J. Perform. Constr. Facil., 2019, 33(1): 04018086, DOI: 10.1061/(ASCE)CF.1943-5509.0001233

Heyman J (1966) The stone skeleton. International Journal of Solids and Structures, **2**(2), 249-279, 1966.

Heyman J (1969) The safety of masonry arches. Int. J. Mech. Sci., 11(4): 363-385

Hendry AW (1998) Structural Masonry. Macmillan: Palgrave Macmillan.

Huerta S (2005) The use of simple models in the teaching of the essentials of masonry arch behavior

Krstevska, L., Tashkov, L., Naumovski, N., Florio, G., Formisano, A., Fornaro, A., Landolfo, R. (2010). In-situ experimental testing of four historical buildings damaged during the 2009 L'Aquila earthquake. COST ACTION C26: Urban Habitat Constructions under Catastrophic Events - Proceedings of the Final Conference, pp. 427-432.

Modena C, Tecchio G, Pellegrino C, da Porto F, Donà M, Zampieri P and Zanini MA (2015) Reinforced concrete and masonry arch bridges in seismic areas: typical deficiencies and retrofitting strategies. Structure and Infrastructure Engineering, 11:4, 415-442, DOI: 10.1080/15732479.2014.951859

Ochsendorf JA (2002) Collapse of masonry structures. University of Cambridge

Oliveira DV, Basilio I and Lourenço PB (2010) Experimental Behavior of FRP Strengthened Masonry Arches J. Compos. Constr., **14**(3): 312-322

Oppenheim IJ (1992) The masonry arch as a four-link mechanism under base motion. Earthq Eng Struct Dynam, **21** (11): 1005-1017

Pelà L, Aprile A and Benedetti A (2013) Comparison of seismic assessment procedures for masonry arch bridges. Constr Build Mater, **38**: 381-394

Pelà L, Aprile A and Benedetti A (2009) Seismic assessment of masonry arch bridges. Eng Struct, **31**(8): 1777-1788

Sarhosis V, Bagi K, Lemos JV, Milani G, (2016a) Computational modeling of masonry structures using the discrete element method. USA: IGI Global.

Sarhosis V, De Santis S, di Felice G (2016b) A review of experimental investigations and assessment methods for masonry arch bridges. Structure and Infrastructure Engineering, **12**(11): 1439-1464.

Sarhosis V, Asteris P, Wang T, Hu W, Han Y. (2016c) On the stability of colonnade structural systems under static and dynamic loading conditions. Bulletin of Earthquake Engineering, 14(4), 1131-1152.

Sarhosis V. and Sheng Y. 2014. Identification of material parameters for low bond strength masonry, Engineering Structures, 60, pp. 100-110.

Stockdale G (2016) Reinforced stability-based design: a theoretical introduction through a mechanically reinforced masonry arch. International Journal of Masonry Research and Innovation, **1**(2): 101-142.

Stockdale G and Milani M (2018a) Diagram based assessment strategy for first-order analysis of masonry arches. J. of Building Engineering, **22**: 122-129.

Stockdale G and Milani M (2018b) Interactive MATLAB-CAD limit analysis of horizontally loaded masonry arches. 10th IMC Conference Proceedings, International Masonry Society. 208-306.

Stockdale G, Sarhosis V and Milani G (2018) Increase in seismic resistance for a dry joint masonry arch subjected to hinge control. 10th IMC Conference Proceedings, International Masonry Society. 968-981

Stockdale G, Tiberti S, Camilletti D, Papa G, Habieb A, Bertolesi E, Milani G and Casolo S (2018) Kinematic collapse load calculator: Circular arches. SoftwareX. 7: 174-179.

Tralli A, Alassandri C and Milani G (2014) Computational methods for masonry vaults: a review of recent results. *Open Journal of Civil Engineering*, **8**(1): 272-287

Zampieri P, Zanini MA, Modena C (2015) Simplified seismic assessment of multi-span masonry arch bridges. Bull Earthq Eng, **13**(9): 2629-2646